The Astrophysical Journal, 951:41 (17pp), 2023 July 1 https://doi.org/10.3847/1538-4357/acd3f0

Inferences from Surface Brightness Fluctuations of Zwicky 3146 via the Sunyaev–Zel'dovich Effect and X-Ray Observations

Charles E. Romero[1], Massimo Gaspari[2], Gerrit Schellenberger[1], Tanay Bhandarkar[3], Mark Devlin[3], Simon R. Dicker[3], William Forman[1], Rishi Khatri[4], Ralph Kraft[1], Luca Di Mascolo[5,6,7], Brian S. Mason[8], Emily Moravec[9], Tony Mroczkowski[10], Paul Nulsen[1,11], John Orlowski-Scherer[3], Karen Perez Sarmiento[3], Craig Sarazin[12], Jonathan Sievers[13], and Yuanyuan Su[14]

[1] Center for Astrophysics, Harvard & Smithsonian, 60 Garden Street, Cambridge, MA 02138, USA; charles.romero@cfa.harvard.edu
[2] Department of Astrophysical Sciences, Princeton University, 4 Ivy Lane, Princeton, NJ 08544-1001, USA
[3] Department of Physics and Astronomy, University of Pennsylvania, 209 South 33rd Street, Philadelphia, PA 19104, USA
[4] Tata Institute of Fundamental Research, Homi Bhabha Road, Mumbai 400005, India
[5] Department of Physics, University of Trieste, via Tiepolo 11, I-34131 Trieste, Italy
[6] INAF—Osservatorio Astronomico di Trieste, via Tiepolo 11, I-34131 Trieste, Italy
[7] IFPU—Institute for Fundamental Physics of the Universe, Via Beirut 2, I-34014 Trieste, Italy
[8] National Radio Astronomy Observatory, 520 Edgemont Rd., Charlottesville, VA 22903, USA
[9] Green Bank Observatory, 155 Observatory Road, Green Bank, WV 24944, USA
[10] ESO—European Southern Observatory, Karl-Schwarzschild-Str. 2, D-85748 Garching b. München, Germany
[11] ICRAR, University of Western Australia, 35 Stirling Hwy, Crawley, WA 6009, Australia
[12] Department of Astronomy, University of Virginia, 530 McCormick Road, Charlottesville, VA 22901, USA
[13] Department of Physics, McGill University, 3600 University Street Montreal, QC, H3A 2T8, Canada
[14] Department of Physics and Astronomy, University of Kentucky, 505 Rose Street, Lexington, KY 40506, USA
Received 2022 October 13; revised 2023 April 24; accepted 2023 May 8; published 2023 July 3

Abstract

The galaxy cluster Zwicky 3146 is a sloshing cool-core cluster at $z = 0.291$ that in Sunyaev–Zel'dovich (SZ) imaging does not appear to exhibit significant pressure substructure in the intracluster medium. We perform a surface brightness fluctuation analysis via Fourier amplitude spectra on SZ (MUSTANG-2) and X-ray (XMM-Newton) images of this cluster. These surface brightness fluctuations can be deprojected to infer pressure and density fluctuations from the SZ and X-ray data, respectively. In the central region (Ring 1, $r < 100'' = 440$ kpc, in our analysis), we find fluctuation spectra that suggest injection scales around 200 kpc (∼140 kpc from pressure fluctuations and ∼250 kpc from density fluctuations). When comparing the pressure and density fluctuations in the central region, we observe a change in the effective thermodynamic state from large to small scales, from isobaric (likely due to the slow sloshing) to adiabatic (due to more vigorous motions). By leveraging scalings from hydrodynamical simulations, we find an average 3D Mach number ≈0.5. We further compare our results to other studies of Zwicky 3146 and, more broadly, to other studies of fluctuations in other clusters.

Unified Astronomy Thesaurus concepts: Galaxy clusters (584); Intracluster medium (858)

1. Introduction

The dominant baryonic component of galaxy clusters is the hot intracluster medium (ICM), which can be observed via X-rays and in the millimeter band via the Sunyaev–Zel'dovich (SZ) effect (Sunyaev & Zel'dovich 1970, 1972). The observed radiative signatures at the two wavelengths' regimes both depend on thermodynamic properties integrated along the line of sight (the gas is optically thin in both regimes), with X-ray surface brightness being roughly proportional to the square of gas density integrated along the line of sight and the millimeter surface brightness being proportional to electron pressure along the line of sight. Temperatures can then be inferred from X-ray spectra or by combining pressure constraints from SZ data with density constraints from X-ray data (e.g., Bourdin et al. 2017; Romero et al. 2017).

Cluster masses can be estimated assuming hydrostatic equilibrium from radial profiles of gas density and profiles of either gas temperature or pressure. The mass inferred under the assumption of hydrostatic equilibrium is expected to fall below the true mass of the cluster by 10%–30% (e.g., Hurier & Angulo 2018). This offset from the true mass is termed "hydrostatic bias" and is expected to be primarily due to nonthermal pressure support, in particular turbulent motions driven by mergers and feedback tied to active galactic nuclei (AGNs; for a review, see Gaspari et al. 2020).

The extent to which the nonthermal pressure is dominated by velocity fluctuations of the gas can be revealed through Doppler broadening of emission lines observed by upcoming X-ray missions with high spectral resolution such as XRISM (XRISM Science Team 2020) and Athena (Nandra et al. 2013; Roncarelli et al. 2018). Fluctuations in thermodynamic quantities may reveal the nature of hydrostatic bias. In particular, pressure fluctuations ($\delta P/P$) can quantify the relative nonthermal pressure of the thermal gas.[15]

To quantify fluctuations as a function of scale, we use amplitude spectra leveraging in the Fourier domain (e.g., Churazov et al. 2012; Gaspari & Churazov 2013; Gaspari et al. 2014). As in previous studies, the amplitude spectrum is

[15] It is often expected that (quasi) turbulent motions dominate the nonthermal pressure, though cosmic rays and magnetic fields may also contribute to the nonthermal pressure.

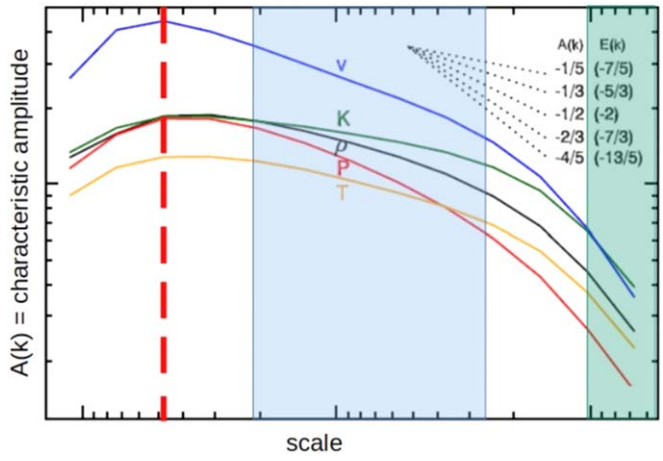

Figure 1. Figure adapted from Gaspari et al. (2014) showing typical ICM amplitude spectra for the thermodynamic relative fluctuations: density ($\delta\rho/\rho$), temperature ($\delta T/T$), entropy ($\delta K/K$), pressure ($\delta P/P$), and velocity $\delta v/c_s$. Smaller scales (distances) are toward the right of the plot; values are suppressed to allow for generalization, i.e., for an arbitrary injection scale, we expect the same shape (roughly) for the spectra, with the peak of the spectra at said injection scale. The red dashed line indicates the injection scale. The shaded blue region indicates the scales over which the fluctuations "cascade" toward smaller scales, and the shaded green region is where the fluctuations are finally dissipated. The dotted black lines help guide the eye as to the (logarithmic) slope of the various spectra, which again should not be treated as an exact expectation; the slopes will vary depending on the actual conditions of the ICM in a given cluster.

defined as

$$A(k) \equiv \sqrt{P(k) 4\pi k^3}, \quad (1)$$

where $k = \sqrt{k_x^2 + k_y^2 + k_z^2}$ and $P(k)$ is the power spectrum. Figure 1 has been adapted from Gaspari et al. (2014) to highlight key features/regions of interest in the amplitude spectra of thermodynamic fluctuations or velocity fluctuations ($\delta v/c_s$, where c_s is the sound speed) when considering a single dominant injection mechanism. In particular, Figure 1 illustrates three important length scales (or range of scales): an injection scale, $l_{\rm inj}$ (e.g., for mergers, expected to be several hundreds of kiloparsecs), intermediate scales (~10–100 kpc) at which the fluctuations are "cascading" toward smaller scales, and small scales at which the fluctuations are gradually dissipated, e.g., via Coulomb collisions or Alfvén/whistler waves (e.g., Drake et al. 2021; Cho et al. 2022). The values in Figure 1 are suppressed to allow for generalization, i.e., the injection scale used in the particular simulation(s) may not match those in a particular cluster, e.g., Zwicky 3146, but we still expect the same general shape of the amplitude spectra (or the summation of such spectra if there are multiple injection mechanisms). The amplitude of the relevant fluctuations is generally taken as the maximum of the amplitude spectrum, $A_{\rm 3D}(k_{\rm peak})$. The scales at which the damping occurs are generally expected to be smaller than can be (spatially) resolved for most galaxy clusters.

Most of the previous studies focused on retrieving the amplitude spectrum of a galaxy cluster using solely X-ray observations (e.g., Schuecker et al. 2003; Churazov et al. 2012; Sanders & Fabian 2012; Gaspari et al. 2013; Zhuravleva et al. 2014; Arévalo et al. 2016). Similar studies have also targeted the amplitude/variance of fluctuations (e.g., Hofmann et al. 2016; Eckert et al. 2017). However, pure X-ray observations are often limited to less than a decade in spatial scale—and mostly targeting density fluctuations. To overcome such limitations, a multi-wavelength approach is required. As a first exploratory study, Khatri & Gaspari (2016) showed that SZ images (via Planck) are a key complementary tool to X-ray data sets, in particular expanding our knowledge of relative ICM fluctuations over the large scales (low Fourier k modes) and the pressure variable. Here, we continue such a multiwavelength approach by leveraging the capabilities of MUSTANG-2.

In this paper, we present a study of surface brightness fluctuations of SZ and X-ray maps of Zwicky 3146, also referred to as ZwCl 1021.0+0426, and associated amplitude spectra covering a decade in scales. Zwicky 3146 ($z = 0.291$, Allen et al. 1992) is a massive, relaxed, sloshing cluster with a cool core (Forman et al. 2002). The relaxed and regular nature of Zwicky 3146 give us the expectation that we will not find large pressure fluctuations. This work is a follow-up to the study of Zwicky 3146 presented in Romero et al. (2020) (wherein Zwicky 3146 is also described in more detail). In particular, Romero et al. (2020) estimated the mass of Zwicky 3146 from pressure profiles determined from high-resolution SZ data and varying assumptions, including hydrostatic equilibrium when combined with electron density profiles determined from XMM-Newton data. Masses from Romero et al. (2020) and references therein (e.g., Martino et al. 2014; Hilton et al. 2018; Klein et al. 2019) are in agreement with $M_{500} = 8 \times 10^{14} M_\odot$, which corresponds to $R_{500} = 5'$ (1.3 Mpc).

The layout of this paper is as follows. Section 2 describes the data used and fitted surface brightness models. To perform our fluctuation analysis, detailed in Section 3, we calculate power spectra on fractional residual maps; that is, residual maps divided by their respective surface brightness models. We present the 2D and (deprojected) 3D amplitude spectra in Section 4, and we discuss them in the context of what is known about Zwicky 3146 in Section 5. We offer conclusions in Section 6.

Throughout this paper, we adopt a concordance cosmology: $H_0 = 70$ km s^{-1} Mpc^{-1}, $\Omega_M = 0.3$, and $\Omega_\Lambda = 0.7$. We define $h_{70} \equiv H_0$ (70 km s^{-1} Mpc^{-1})$^{-1}$ and $h(z) \equiv H(z) H_0^{-1}$. At the redshift of Zwicky 3146 ($z = 0.291$), one arcsecond corresponds to 4.36 kpc.

2. Data Products

We make use of MUSTANG-2 data presented in Romero et al. (2020) and archival XMM-Newton EPIC data. The two data sets are highly complementary. MUSTANG-2 has a resolution (full width half maximum; FWHM) of ~10″. The point-spread function (PSF) of each of XMM-Newton's detectors, MOS1, MOS2, and pn, depends on the energy, and off-axis distance; for a point of rough comparison, we may consider that the detectors have an effective resolution of ~5″, albeit with broad wings.

2.1. MUSTANG-2 Data Products

MUSTANG-2 is a 215 detector array on the 100 m Robert C. Byrd Green Bank Telescope (GBT) and achieves 10″ resolution (FWHM) with an instantaneous field of view (FOV) of 4.′2. Observing at 90 GHz, it is sensitive to the SZ

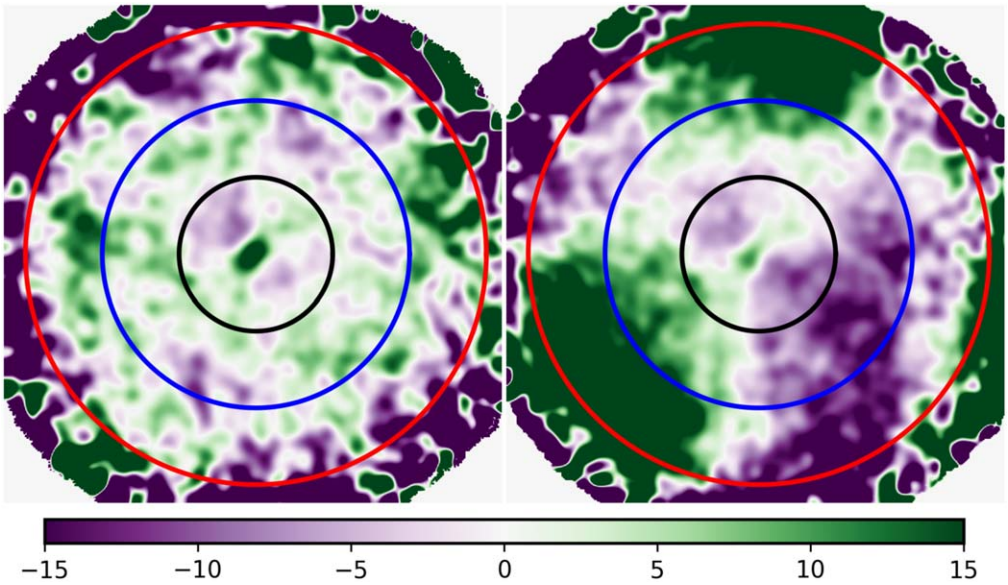

Figure 2. Maps derived from the MUSTANG-2 observations: the residual Minkasi map (right) shows large-scale noise, while the residual MIDAS map (left) has this filtered out. Given the angular scales of interest, the MIDAS map is preferable. The rings are as in Figure 5. The color scale is shown in units of $y \times 10^6$; y is defined in Equation (2).

effect, which is often parameterized in terms of Compton y:

$$y = \frac{\sigma_{\rm T}}{m_{\rm e}c^2} \int P_e(\theta, z) dz, \tag{2}$$

where $\sigma_{\rm T}$ is the Thomson cross section, m_e is the electron mass, c the speed of light, P_e the electron pressure, and z the axis along the line of sight.

The observations used here are the same as in Romero et al. (2020), as is the general data reduction. We employ both data reduction pipelines, MIDAS and Minkasi, in this work. Briefly, MIDAS follows a more traditional approach in its data processing (i.e., similar to the processing of many predecessor multipixel bolometric ground-based measurements); this processing typically restricts scales recovered (often characterized as a transfer function)[16] to less than the instrument's instantaneous FOV (see Figure 2). Meanwhile, Minkasi fits the data in the time domain and does not suffer the same loss of scales as MIDAS; see Romero et al. (2020) for a detailed comparison of the transfer functions of the two processing methods.

In this work, we update our pressure profile model from Romero et al. (2020) with an additional procedure used in Dicker et al. (2020) and Orlowski-Scherer et al. (2022), which attempts to further remove atmospheric contributions to our maps by fitting and subtracting a second-order polynomial with respect to elevation offset from the scan center. Figure 3 compares the current to the former pressure profile; the two are fully consistent with each other. As reported in Romero et al. (2020), the two pressure profile models (fit via MIDAS and Minkasi) are consistent, except beyond MUSTANG-2's radial (instantaneous) FOV where our transfer function is poorly constrained. However, when we subtract the Minkasi model via the MIDAS pipeline (rather than using a transfer function), we see that the residual map is consistent with noise at the radii where the pressure profiles (MIDAS versus Minkasi) differ.

[16] The transfer function as used in Romero et al. (2020) is quantified as the transmission of the Fourier transform of an input map.

2.2. XMM Data Products and Models

There are four XMM-Newton observations (Obs.IDs) of Zwicky 3146: 0108670401, 0108670101, 0605540301, and 0605540201. The first does not have usable EPIC data; we use the remaining three observations (of nominal durations 56, 65, and 123 ks; see also Table 1).

We use heasoft v6.28 and SAS 19.0 and the Extended Source Analysis Software (ESAS) data reduction package (Snowden et al. 2008) to produce event files and eventually images for the three EPIC detectors: MOS1, MOS2, and pn. Our data reduction largely follows the ESAS cookbook,[17] with the initial steps being `emchain`, `epchain`, and `epchain withoutoftime = true` to extract calibrated events files. Soft proton flares are excised with the tasks `mos-filter` and `pn-filter`. A comparison of IN versus OUT count rates assesses the amount of residual contamination from soft protons (De Luca & Molendi 2004). This comparison suggests that soft protons are not a concern for MOS detectors and that the pn detectors could suffer slight contamination.

An initial list of point sources is created with the task `cheese` on the XMM-Newton data set based on flux with [0.4–7.2] keV energy band and detection significance. A region file is generated, excluding a 30″ radius about each point source.

2.2.1. Image Creation

We choose to extract images in the [0.4–1.25] keV and [1.25–5.0] keV bands. Images and vignetted exposures are extracted for each detector over the entire detector area while masking point sources (see Section 2.2.3 for point-source identification) via the task `mos-spectra` or `pn-spectra`. Unvignetted exposures are also created with the task `eexpmap withvignetting = no`. Wideband (i.e., [0.4–5.0] keV) images are formed by the simple addition of the count (and

[17] https://heasarc.gsfc.nasa.gov/docs/xmm/esas/cookbook/xmm-esas.html

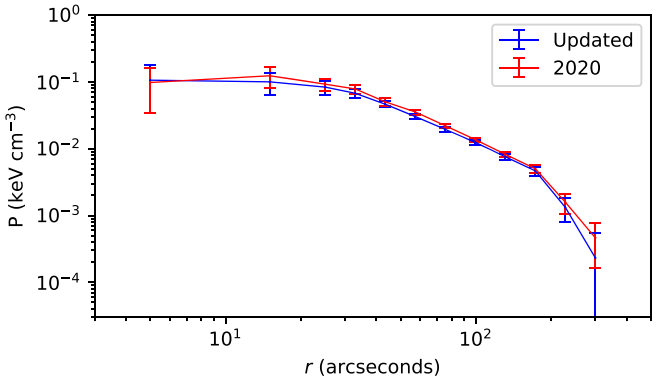

Figure 3. Our updated profile is consistent with our previously published profile; we do see the outermost bin has a lower pressure than previously (Romero et al. 2020).

Table 1
Overview of Imaging XMM-Newton Observations of Zwicky 3146

Obs ID	0108670101	0605540301	0605540201
Date	2000 Dec 5	2009 May 8	2009 Dec 13
Exposure (ks)	56.5	64.9	122.8
Clean Exp (ks)	MOS1: 51.2 MOS2: 51.7 pn: 43.3	MOS1: 41.8 MOS2: 40.6 pn: 29.6	MOS1: 101.2 MOS2: 102.2 pn: 73.8
Mode	FF	eFF	eFF
PI	R. Mushotzky	J. Sanders	J. Sanders

Note. Modes FF and eFF are "Full Frame" and "extended Full Frame," respectively.

background) images; these wideband images are used for consistency checks.

2.2.2. Constrained Background Components

The relevant particle backgrounds are calculated for the desired energy band via the tasks `mos_back` and `pn_back`. For the pn detector, we extract a separate spectrum (via `pn-spectra`) over the cluster region, which we take to be a radius of 5′ about the cluster center. While we treat the residual soft proton spectrum as a single power law, we must fit several other components to the spectrum: a thermal plasma component (`apec`) for each of the local (solar) hot bubble, Galactic emission, and the ICM in Zwicky 3146. In addition to this, we also consider Gaussian components for fluorescent lines. A soft proton background is then made with the task `proton` and added to the particle background with the task `farith`. For the pn detector, we also consider the out-of-time (OOT) contribution. Depending on the full-frame mode, we multiply our resultant pn image with randomized columns by 0.063 or 0.023 for full-frame and extended-frame modes, respectively, to have an OOT component that we incorporate into the pn background. These background images will be subtracted from the respective images when extracting profiles.

2.2.3. Point-source Exclusion

In addition to the list generated from `cheese`, we make use of Chandra archival data of Zwicky 3146 and run `wavdetect` on its calibrated event files. Finally, we perform a manual inspection to identify any remaining point sources.

2.2.4. Profile Fitting

We use the Python package `pyproffit` (Eckert et al. 2017) to extract profiles of our images. Profiles are fit via `emcee` (Foreman-Mackey et al. 2013) separately for each detector, each energy band, and each observation. We fit profiles to our low-energy ([0.4–1.25] keV) and high-energy ([1.25–5.0] keV) images. As these profiles are fit per detector and per ObsID, we have 18 profiles in total (with another nine from the wide-energy-band [0.4–5.0] keV images that are only used for consistency checks).

Beyond masking the point sources, we also introduce a mask to exclude pixels of low exposure due to binning near chip gaps. We allow `pyproffit` to fit for centroids in the central 5′ of each (masked) image independently. Within a single observation and energy band, the centroids of each detector differ by $\lesssim 2''$. Given the general agreement, for each observation and energy band, we adopt circular symmetry and the centroid as the average centroid of the maps from each EPIC camera detector when extracting profiles. To be sure, the centroids determined in this manner differ by $\sim 3''$ relative to the centroid used with MUSTANG-2 analysis.

We find that a simple β-model does not sufficiently capture the surface brightness in the core of Zwicky 3146 and at large radii. We adopt the double β-model as implemented in `pyproffit`, which has the form

$$S(r) = S_0[(1 + (r/r_{c,1})^2)^{-3\beta+0.5} + R(1 + (r/r_{c,2})^2)^{-3\beta+0.5}] + B, \quad (3)$$

where r is the radius, $r_{c,1}$ is the first "core" (scaling) radius, $r_{c,2}$ is the second "core" (scaling) radius, R is a ratio between the two β-profile components, S_0 is the surface brightness normalization, and B is the background. We modify the background component (taken to be uniform in `pyproffit`) to be two components: one uniform and one the scaling of unvignetted-to-vignetted exposure maps. This latter component allows us to capture the contribution from fluorescent lines, predominantly the line from aluminum, which is evident in the extracted profiles seen in Figure 4.

To appropriately constrain these background components, we find that we should fit (from $r = 0$) out to at least 10′, but beyond 10′ the values of the background components do not change much. We choose 11′ (more than $2R_{500}$) as our fitting region. Across all three observation IDs, detectors, and energy bands, the profile residuals are quite small, as in Figure 4.

We find that the residuals of the double β-model are generally very small, with slightly larger residuals toward the core where known sloshing exists (e.g., Forman et al. 2002). We find that this is not a shortcoming of the double β-model, per se, but rather affirmation that the surface brightness of the cluster, while roughly circular at large radii, is not circular in the core (see axial ratios found in Romero et al. 2020).

3. Power Spectra Measurements

To quantify the fluctuations in surface brightness, we want to take the power spectra of residual images divided by the corresponding ICM surface brightness model as shown in Figure 5. We term these images "fractional residuals," and they are designated by either $\delta S/S$ for X-ray images or $\delta y/y$ for SZ images. In particular, Figure 5 shows fractional residual maps for MUSTANG-2 and pn images from a single observation in

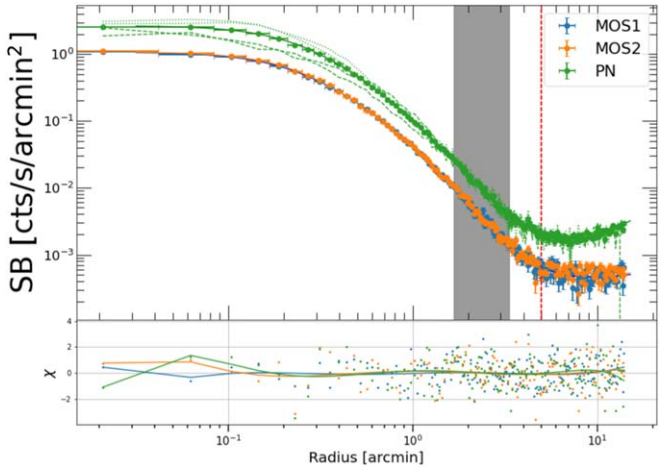

Figure 4. Profile fits of circular double β-models to each detector array in our "high-energy" (1250–5000 eV) band for observation ID 0605540201. The gray vertical band is between 100″ and 200″, i.e., the region used for Ring 2. The vertical red line is at 300″ ($\sim R_{500}$ and the outer edge of Ring 3). The dotted and dashed green curves show the PN profile broken into quadrants (along cardinal directions). The dotted lines are the two western quadrants, and the dashed lines are the eastern quadrants. The lines in the residual are a polynomial regression to indicate large-scale residuals.

the 400–1250 and 1250–5000 eV bands. From these (2D) spectra of the images, we can deproject to spectra of underlying 3D thermodynamical quantities, namely pressure for SZ images and density for X-ray images (see Section 3.3).

Motivated in part by the data, as well as by the theoretical expectation for differing levels of fluctuations as a function of cluster-centric radii, we divide the cluster into three annuli:

1. Ring 1: $r < 100'' = 440$ kpc.
2. Ring 2: $100'' < r < 200''$.
3. Ring 3: $200'' < r < 300'' = R_{500}$.

We also note that the MUSTANG-2 map has a rapidly increasing rms beyond 200″, while the rms is nearly uniform within 100″.

We calculate the power spectra of the fractional residual images, P_{2D}, at five angular scales spaced logarithmically between 10″ (the FWHM of MUSTANG-2) and 100″ (the radial width of our annuli, i.e., rings). Corresponding amplitude spectra, A_{2D} and A_{3D}, are given as

$$A_{2D}(k) = [k^2 P_{2D} * (2\pi)]^{1/2}, \quad (4)$$

$$A_{3D}(k) = [k^3 P_{3D} * (4\pi)]^{1/2}. \quad (5)$$

We use a modified Δ-variance method (Arévalo et al. 2012) to calculate the power spectra of surface brightness fluctuations. In particular, this method allows us to recover power spectra of data with arbitrary gaps (masks) in (of) the data, which suits our needs well. We do, however, need to be cautious of the bias that can occur due to steep underlying spectra; this is especially true given that we will attempt to recover spectra up to scales close to the FWHM of MUSTANG-2 and XMM. In particular, the convolution of a moderate slope with the PSF for either MUSTANG-2 or any of the EPIC cameras will lead to not only a steep slope but a changing steep slope. The bias for this changing slope is derived in Appendix B. While we report spectral values at $k = 0.1$ arcsec^{-1} in later figures, this bias and associated uncertainty reduces the significance of the values at $k = 0.1$ arcsec^{-1} such that none of them is statistically significant.

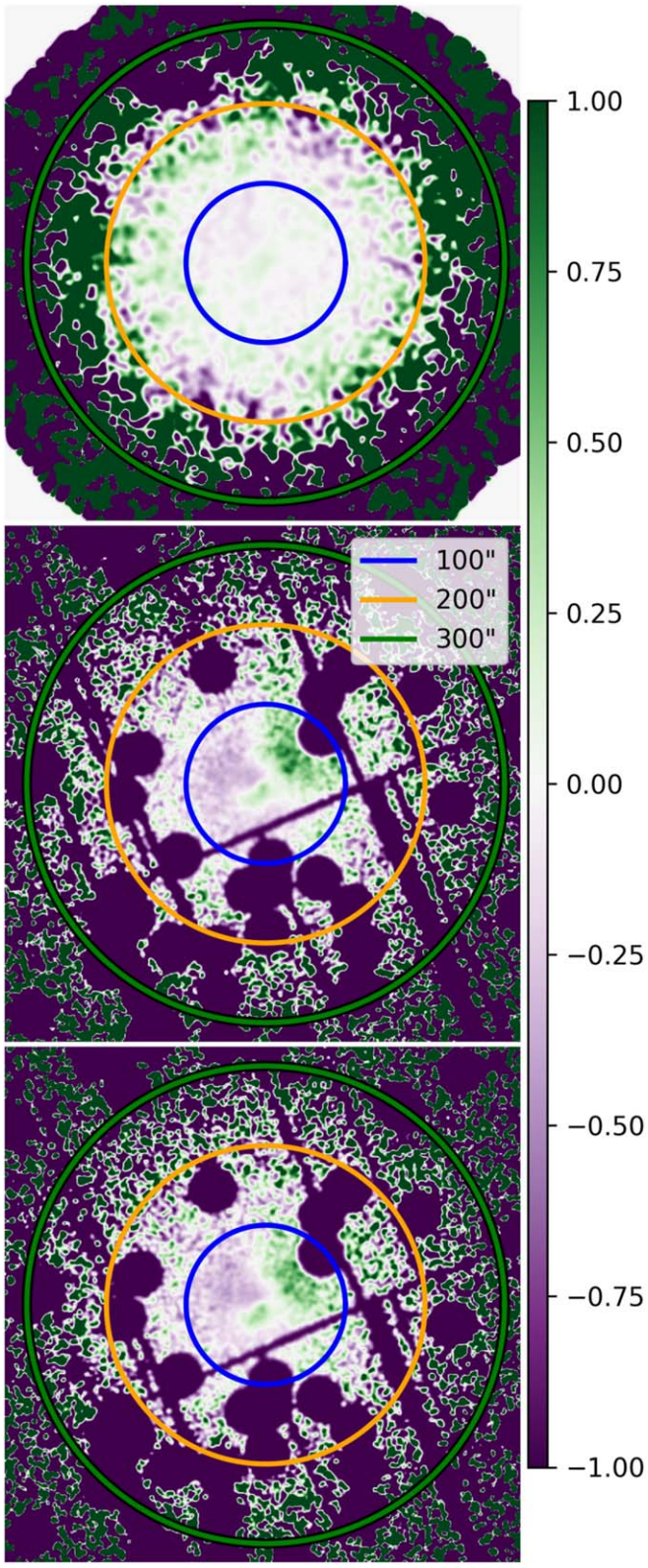

Figure 5. Fractional residuals of our MUSTANG-2 data (upper) and XMM-Newton data (only pn chip from observation 0605540201 shown) in the middle (400–1250 eV) and bottom (1250–5000 eV). The blue, orange, and green circles indicate $r = 100''$, 200″, and 300″, respectively. The purple lines and circles are masked chip gaps and point sources.

3.1. Calculations on MUSTANG-2 Data

As noted in Section 2.1, our MUSTANG-2 residual map is created by subtracting the best-fit model (from Minkasi) within

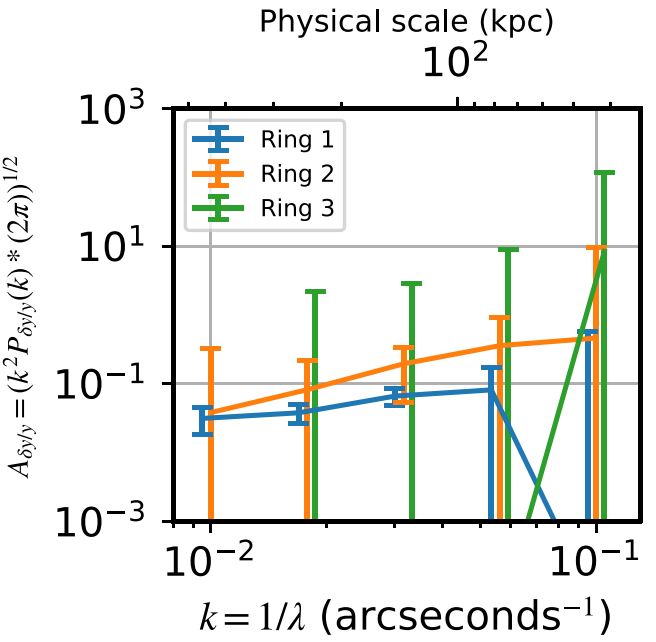

Figure 6. The amplitude spectrum of the fractional residual ($\delta y/\bar{y}$) for each ring. Abscissa values are offset between rings for visual separation. Our best constraints are in Ring 1, while Ring 2 is already quite noisy.

the MIDAS pipeline. In all, 155 scans on source are used. Maps are produced for each scan, and the final residual image (see again Figure 5, top panel) is constructed as the (weighted) sum of these individual scan maps.

In order to calculate power spectra due to the ICM, we must account for any power contribution from inherent noise in the maps. In principle, this can be done by "debiasing" the power spectrum (as will be described in Section 3.2), but a more direct method is to "halve" the data and take a cross-spectrum (e.g., see Khatri & Gaspari 2016). However, instrumental noise can still "leak" through via such a cross-spectrum. In order to counter this, we calculate cross-spectra of noise realizations, which have amplitudes $\lesssim 1/10$ the amplitudes of signal cross-spectra, and in effect, they debias the cross-spectra. We perform both methods on the SZ data, and present the results of the cross-spectra calculations in Figure 6. For the cross-spectra calculation, we take halving to be the generation of two maps covering the same area, each with half of the weight of a "full" map.

Division in half is not a trivial endeavor, as these scans were taken over seven nights of observations, and even the nights with the best observing conditions had some variation in weather conditions. As such, we opt to create two halves randomly, 100 times. Cross-spectra are calculated on these 100 pairs, and the presented values are taken as the mean of the resultant spectra with their associated standard deviations. The 2D amplitude spectra, A_{2D}, for the MUSTANG-2 data are shown in Figure 6, and they include corrections for the MUSTANG-2 beam (PSF; the correction is shown as the dashed gray line) and MIDAS transfer function, both of which are characterized in Romero et al. (2020).

As mentioned earlier, we also calculated spectra via the debiasing route. The spectra in each ring are statistically consistent between the two calculation methods; however, Ring 2 is statistically consistent with zero, as calculated via debiasing. Similarly, the spectrum in Ring 3 has negligible significance, and thus we discard it from further analysis.

3.2. Calculation on XMM Data

In order to calculate the power spectra for our XMM images, we opt to debias our spectra as calculated directly on maps of fractional residuals. A noise realization can be generated as Poisson noise realizations for each pixel, with its expected value given by a model of expected counts of all relevant components. To also incorporate uncertainties from the surface brightness model itself, we take 1000 models from the MCMC chains well after the burn-in. A single Poisson noise realization is generated for each of these models. The "raw" and "noise" spectra are recorded for each, as well as their difference (i.e., a "debiased" spectrum). The mean and standard deviation of these debiased spectra are used in reported expected values and associated uncertainties.

We also consider the potential contribution of faint point sources below our detection threshold. To account for these, we quantify the distribution of detected sources in our images. We normalize a Log N–Log S distribution with an index of -1.6 (Mateos et al. 2008) to our bright sources, where we take our completeness to be unity. We then randomly generate point sources of this distribution down to a minimum of one photon (count) when assuming a uniform (unvignetted) exposure. The final point-source image, added to a noise realization, accounts for the proper (vignetted) exposure map. To stay consistent with total count expectations, we assume that the counts accumulated from these faint point sources would be equivalent to the uniform background (in count rates) in our profile fits. As such, we reduce the uniform background by the equivalent count rates.

Given the general agreement between energy bands (see Figure 7), we conclude that it is appropriate to take the weighted average of the respective power spectra, as shown in Figure 8. When checking power spectra across individual observations and detectors, we do not find any spurious spectra. However, we also note that Figure 7 provides some insights into data quality, especially suggesting caution when attempting to interpret the combined amplitude spectrum in Ring 3 as well as the highest k-mode in all rings.

Both Figures 7 and 8 include corrections for the PSF, which we estimate per detector, per energy band, and per ring, using the `ELLBETA` mode of the task `psfgen`. In particular, we find the median photon energies are 800 and 2000 eV for our two energy bands, and so we estimate the PSF at those energies. For the rings, we take $x = 50''$, $150''$, and $250''$, and $y = 0$ to be sufficient estimates of the PSFs for each ring. As in the SZ data, we see that some rings have (at least a portion of their) spectra that share the shape of the PSF correction.

To further investigate the quality in Ring 3, we calculate the radial profile (from the cluster center) of variance in the $\delta S/S$ images. We find that the average variance falls below the standard deviation of the variance (across our 1000 realizations, three detectors, two energy bands, and three ObsIDs) beyond $200''$.

3.3. 3D Spectra

In this section, we relate projected 2D fluctuations to the physical 3D fluctuations by following a common formalism (e.g., Peacock 1999; Churazov et al. 2012; Zhuravleva et al. 2012;

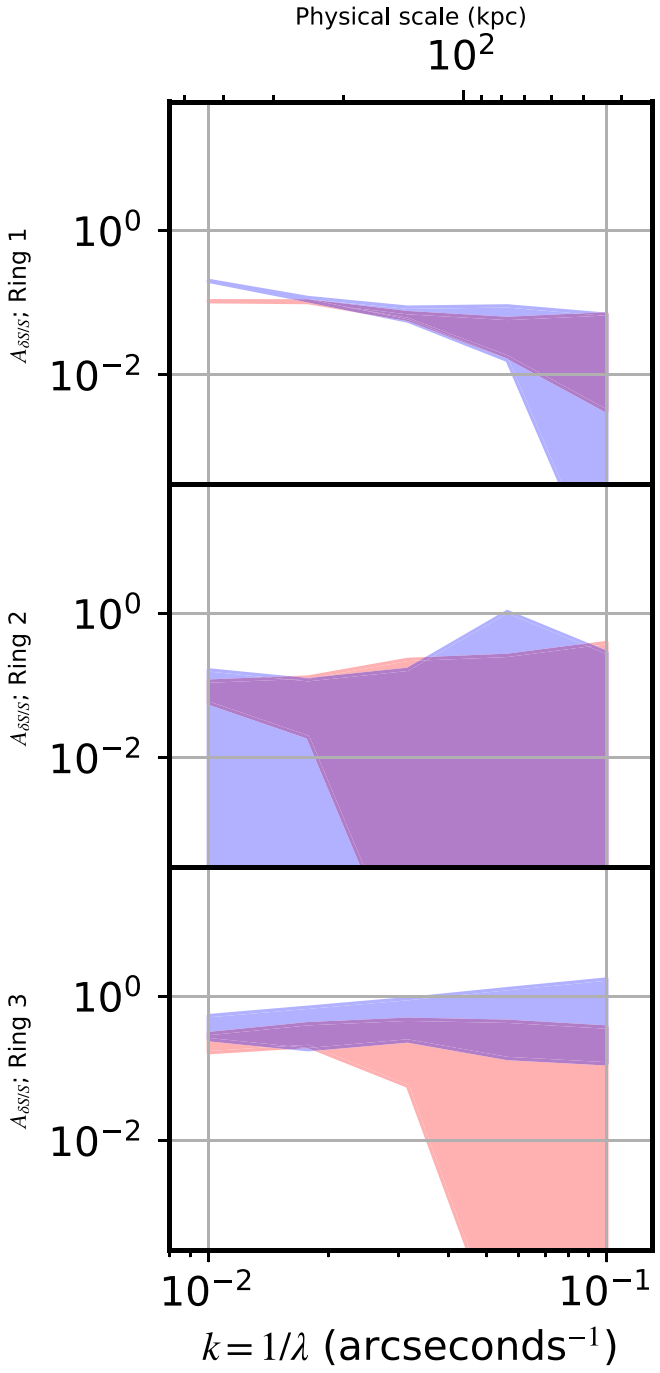

Figure 7. The $\pm 1\sigma$ interval of amplitude spectra for the low-energy band (red) and high-energy band (blue). From top to bottom: Rings 1, 2, and 3, respectively.

Khatri & Gaspari 2016). The relation is given as

$$P_{2D}(k_\theta) = \int P_{3D}(\boldsymbol{k}) |\tilde{W}(k_z)|^2 dk_z, \tag{6}$$

where z is the axis along the line of sight, $\theta^2 = x^2 + y^2$ is in the plane of the sky, and $|\tilde{W}(k_z)|^2$ is the 1D power spectrum of the window function, which normalizes the distribution of the relevant (unperturbed) 3D signal generation to the (unperturbed) 2D surface brightness. Additionally, P_{2D} is as before, and P_{3D} is the power spectrum of the 3D quantity, which when integrated along the line of sight yields a surface brightness.

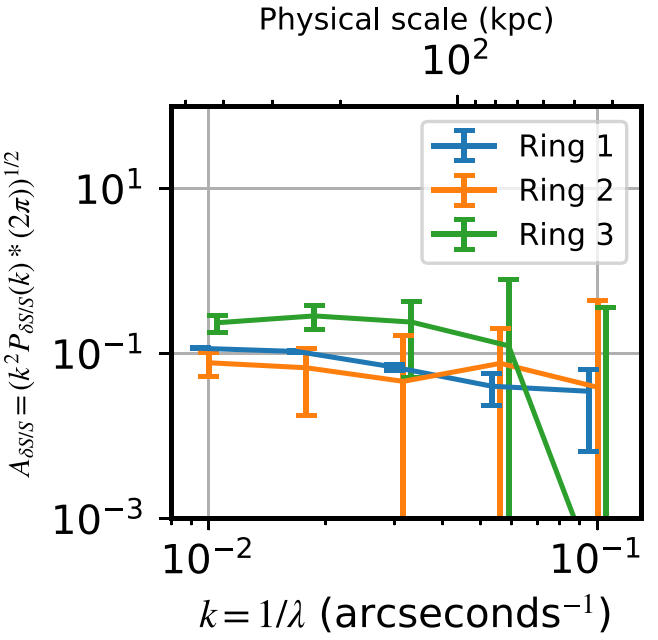

Figure 8. Amplitude spectra of X-ray surface brightness fluctuations when combining both energy bands. Abscissa values are offset between rings for visual separation. Ring 2 has a spectrum similar to that of Ring 1, but with larger uncertainties.

The SZ and X-ray window functions are, respectively:

$$W_{SZ}(\theta, z) \equiv \frac{\sigma_T}{m_e c^2} \frac{\bar{P}(\theta, z)}{\bar{y}(\theta)}, \tag{7}$$

$$W_X(\theta, z) \equiv \frac{\bar{\epsilon}(\theta, z)}{\bar{S}(\theta)}, \tag{8}$$

where $\bar{P}$ and $\bar{\epsilon}$ (emissivity) refer to the underlying 3D (spherical, unperturbed) models, which when integrated along the line of sight produce $\bar{y}$ and $\bar{S}$, the 2D (circular, unperturbed) surface brightness models. To be sure, the relation between $\bar{S}$ and $\bar{\epsilon}$ is given by $\bar{S} = \int \bar{\epsilon} dz$.

Above some cutoff wavenumber, $k_{z,\mathrm{cutoff}}$, $|\tilde{W}(k_z)|^2$ will fall off; in the regime where $k \gg k_{z,\mathrm{cutoff}}$, we can approximate Equation (6) as

$$P_{2D}(k_\theta) \approx P_{3D}(\boldsymbol{k}) \int |\tilde{W}(k_z)|^2 dk_z, \tag{9}$$

where we adopt the notation used in Khatri & Gaspari (2016) and define

$$N(\theta) \equiv \int |\tilde{W}(k_z)|^2 dk_z. \tag{10}$$

In Appendix C, we verify that this approximation in Equation (9) is valid.

The dependence of the window function on the cluster-centric radius, θ, presents an issue of how to deproject over an area (e.g., over a given annulus). We therefore calculate $N(\theta)$ along many points in the range $0'' \leqslant \theta \leqslant 300''$ and calculate an area-weighted average of those values (within a given annulus). Window functions (and their Fourier transform) are shown in Figures 9 and 10; the radii chosen are the effective radii for each annulus (i.e., where $N(\theta_{\mathrm{eff}}) = \langle N(\theta) \rangle$ for r in a given annulus.)

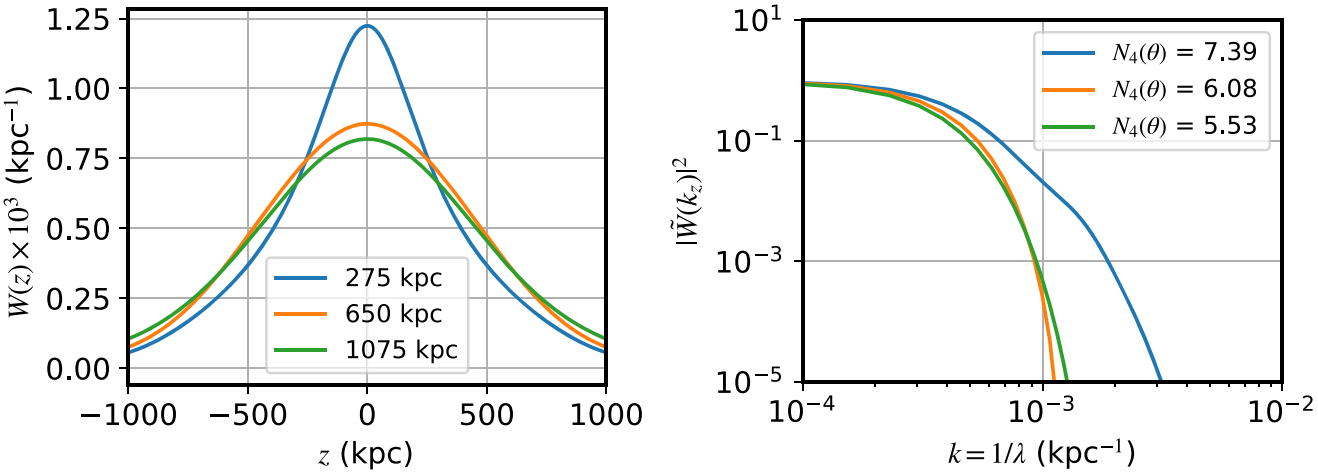

Figure 9. The SZ window function in real space and in Fourier space. $N_4(\theta) = N(\theta) * 1e4$ with units of inverse kiloparsec (see Equation (10)).

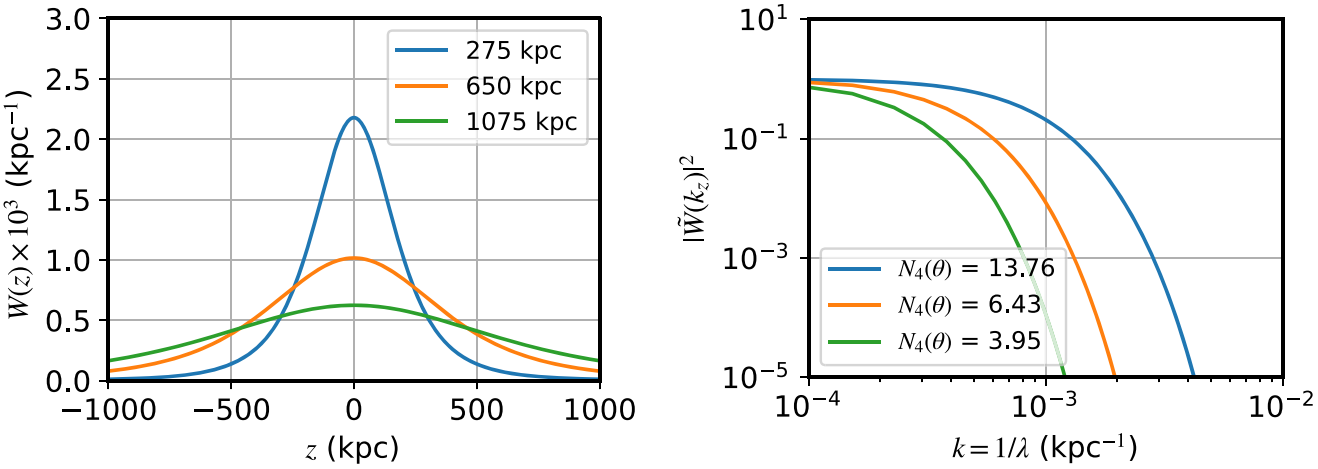

Figure 10. The X-ray window function in real space and in Fourier space. $N_4(\theta) = N(\theta) * 1e4$ with units of inverse kiloparsec (see Equation (10)).

In the SZ case, this deprojection to 3D fluctuations lets us immediately arrive at pressure fluctuations ($\delta P/P$) because it is the thermal electron pressure that is being integrated along the line of sight. However, in the X-ray case, we have only derived a means of converting to fluctuations in emissivity ($\delta\epsilon/\epsilon$). Fortunately, for hot enough gas (~3 keV), the emissivity in soft bands is weakly sensitive to temperature, and thus it effectively depends only on the square of gas density, n. The emissivity can be expressed as $\epsilon = Cn_e^2$, where we include the cooling function and mean molecular weight in C and note that C is weakly dependent on temperature at the temperatures of Zwicky 3146, such that C acts roughly as a constant. The emissivity can be decomposed into unperturbed and perturbed terms and is linearly approximated as $\epsilon = Cn^2[1 + 2\delta_n]$, with δ_n being the density perturbation. This factor of two associated with δ_n ultimately yields a factor of four when relating P_{2D} to $P_{3D,n}$. That is, explicitly for SZ and X-ray, we have

$$P_{\delta y/y}(k_\theta) \approx N_{\theta,\mathrm{SZ}} P_{\delta P/P}(\boldsymbol{k}), \tag{11}$$

$$P_{\delta S/S}(k_\theta) \approx 4N_{\theta,\mathrm{X}} P_{\delta n/n}(\boldsymbol{k}). \tag{12}$$

4. 3D Spectra Results

Given our deprojection approximation, the 3D amplitude spectra, A_{3D}, will simply be the 2D amplitude spectra rescaled by a scalar and multiplied by another factor of k.

As indicated in Section 3.2, the (2D) amplitude spectrum in Ring 3 from X-ray data is likely dominated by noise. We include it in our plot of 3D amplitude spectra (Figure 11) and tabulation of single spectral indices (Table 2), but do not include it in further analyses. Similarly, we exclude Rings 2 and 3 of the SZ data from further analysis (as justified in Section 3.1).

Figure 11 shows the resultant density and pressure fluctuations.

If a clear peak were present in a given spectrum, we could take the amplitude at the peak ($A_{3D}(k_{peak})$) to be the amplitude of the amplitude spectrum. However, as an example, taking the highest k point for Ring 2 (orange) in Figure 11 is also problematic, as it is consistent with zero. That is, choosing a peak is not solely a question of the shape of the spectra, but also of data quality. We wish to select the highest point with some threshold significance; in particular, we adopt 3σ as our threshold significance. The maximum values with at least 3σ significance are reported in Table 2. With this adopted

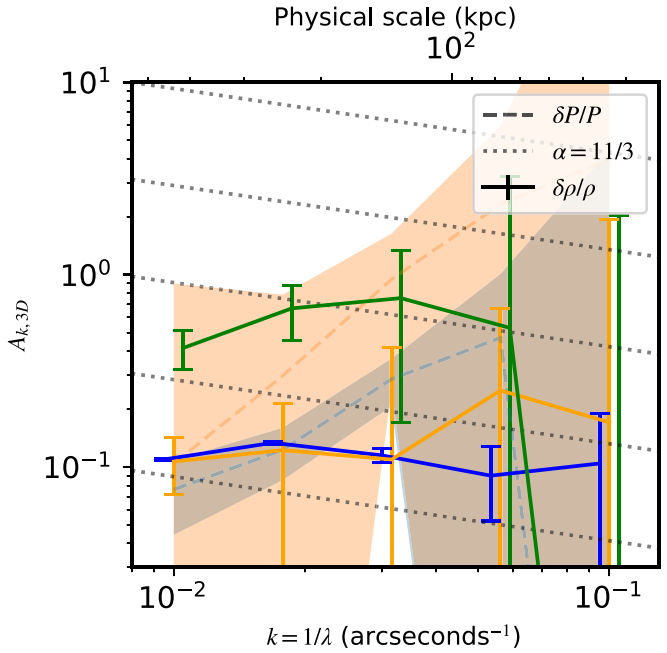

Figure 11. Amplitude spectra of deprojected quantities. Colors reflect corresponding rings as in previous plots of spectra; SZ-derived spectra ($\delta P/P$) are shown as dashed lines and shaded regions, while the X-ray-derived ($\delta n/n$) spectra are shown as lines with error bars. The dotted lines show the spectral indices for the power spectra (following the convention indicated in Equation (13)).

Table 2
Inferred Spectral Indices (Logarithmic Slope) and Peaks of the Amplitude Spectra

		α_k	A_{3D} (k_{peak})	σ_{3D}	k_{peak} ($''^{-1}$)	λ_{peak} (kpc)
Ring 1	$\delta\rho/\rho$	2.5 ± 0.1	0.13 ± 0.003	0.15	0.02	250
	$\delta P/P$	0.6 ± 0.8	0.29 ± 0.08	0.33	0.03	140
Ring 2	$\delta\rho/\rho$	2.2 ± 1.6	0.11 ± 0.03	0.18	0.01	440
Ring 3	$\delta\rho/\rho$	1.7 ± 1.0	0.67 ± 0.21	0.83	0.02	250

Notes. The spectral indices assume a single power-law across our sampled range, with the exception of points at $k = 0.1$ arcsec^{-1} (we omit points at $k = 0.1$ arcsec^{-1}). The peaks of amplitude spectra are taken with a signal-to-noise cut of 3.

significance threshold, we find peaks in the range $0.01 < k < 0.03$, which corresponds to injection scales, ℓ_{inj}, of 140 kpc $< \ell_{inj} <$ 440 kpc.

Though we may expect a changing power law (as in Figure 1), we fit a single power law to our power spectra, omitting $k = 0.01$, and we report the (logarithmic) slope, α, in Table 2, where we use the convention

$$P(k) = P_0 k^{-\alpha}, \tag{13}$$

with P_0 being a normalization of the fitted slope. We note that, without a clear indication that we are sampling below an injection scale, our slopes are not indicative of the cascade of motions to smaller scales. Moreover, with our best estimate of the injection scales (140 kpc $< \ell_{inj} <$ 440 kpc), our constraints on the slope on smaller scales are minimal. These slopes do permit us to comment on the validity of our deprojection approximation (see Appendix C). We can additionally integrate

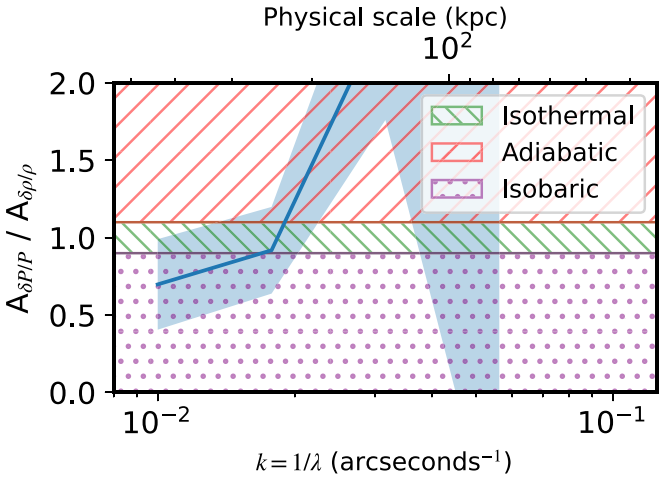

Figure 12. Constraints on the thermodynamical regimes within Ring 1 given the ratio of the 3D amplitude spectra (pressure relative to density). The isothermal regime is taken to be between 0.9 and 1.1, with the adiabatic regime taken to be values above 1.1 and isobaric regime to be values below 0.9.

the power spectra to obtain a measure of the variance of fluctuations; for the 3D spectra, this is given as

$$\sigma_{3D}^2 = \int P(k) 4\pi k^2 dk. \tag{14}$$

We report the values of σ_{3D} in Table 2.

5. Discussion

In the context of expected amplitude spectra (see Section 1 and Figure 1), our recovered spectra do not clearly identify an injection scale and subsequent cascade. From Figure 11, we may loosely infer an injection scale 100 kpc $\lesssim l_{inj} \lesssim$ 300 kpc for Rings 1 and 2. In the core, an injection scale around 50 kpc could be plausible, as Vantyghem et al. (2021) find evidence in Chandra data for cavities with diameters $\lesssim$50 kpc in Zwicky 3146. Hydrodynamical simulations of AGN feedback also support such injection scales (e.g., Wittor & Gaspari 2020). However, the evidence for these cavities does not extend to Ring 2. In Ring 1, we see the density fluctuations increase relative to the pressure fluctuations at the larger scales probed ($\sim$400 kpc), which is consistent with a sloshing core. This also highlights that there may be multiple injection mechanisms (and scales) present in clusters.

In the present study, we refrain from making physical inferences regarding the slopes of the spectra. We do, however, compare the pressure and density spectra (in Ring 1; see Figure 12) as well as infer Mach numbers from our spectra. We note that Hofmann et al. (2016) have performed a fluctuation analysis, though not in the Fourier domain, of a sample of clusters which includes Zwicky 3146. Their analysis probed Zwicky 3146 using Chandra data out to $r \lesssim 90''$, and thus it can be compared to results from our Ring 1. They derive standard deviations for $\delta P/P$ and $\delta\rho/\rho$ of 0.004 and 0.159, respectively.[18] Our respective derived quantities ($\sigma_{\delta P/P}$ and $\sigma_{\delta\rho/\rho}$) are 0.33 and 0.15. Our integrated density fluctuation is in good agreement with that from Hofmann et al. (2016); however, our

[18] The value for $\delta P/P$ (dP/P in their notation) that Hofmann et al. (2016) report in their table is surprisingly low, given the scatter evident in their pressure profile.

integrated pressure fluctuation is considerably larger than those from Hofmann et al. (2016).

5.1. Thermodynamic State

There are three effective thermodynamical regimes to constrain:

$$\text{adiabatic:} \left| \frac{\delta K}{K} \right| \sim 0,$$

$$\text{isothermal:} \left| \frac{\delta T}{T} \right| \sim 0,$$

$$\text{isobaric:} \left| \frac{\delta P}{P} \right| \sim 0,$$

where K is the gas entropy. With γ being the classic adiabatic index, we have the following relations between pressure and density in the respective regimes:

$$\text{adiabatic:} \left| \frac{\delta P}{P} \right| = \gamma \left| \frac{\delta n}{n} \right|, \quad (15)$$

$$\text{isothermal:} \left| \frac{\delta P}{P} \right| = \left| \frac{\delta n}{n} \right|, \quad (16)$$

$$\text{isobaric:} \left| \frac{\delta P}{P} \right| \ll \left| \frac{\delta n}{n} \right|. \quad (17)$$

Assuming $\gamma = 5/3$ for a monatomic gas, we can roughly divide these regimes as shown in Figure 12. The isobaric regime $A_{\delta P/P} < A_{\delta n/n}$ is only observed at the largest scales. This is consistent with the slow perturbations driven by sloshing. Interestingly, we see that the inferred thermodynamical regime shifts to isothermal and adiabatic toward the intermediate scales. The transition from isobaric to the adiabatic state is a sign of more vigorous motions (see Gaspari et al. 2014) as we approach the potential injection scale peak at a few tens of kiloparsecs. It is important to note that the isothermal transitional regime does not necessarily imply strong thermal conduction or cooling, but it is a sign of a change in the effective equation of state, likely due to the varying kinematics at different scales. For instance, Spitzer-like thermal conduction would also substantially suppress the density fluctuations up to a scale of hundreds of kpc (Gaspari et al. 2014), thus generating amplitude spectra with a very steep negative slope in logarithmic space. Our results are also in line with other observational studies (Arévalo et al. 2016; Zhuravleva et al. 2018), which find a mixture of gas equations of state, where Zhuravleva et al. (2018), specifically analyzing a sample of cool-core clusters, find that the gas tends to be isobaric.

5.2. Mach Numbers

In principle, we can infer nonthermal pressure, $P_{\rm NT}$, support and ultimately a hydrostatic bias, usually defined as

$$b \equiv 1 - M_{\rm HSE}/M_{\rm tot}, \quad (18)$$

from our amplitude spectra presented in Section 4, where we make the assumption that the nonthermal pressure support comes from (quasi) turbulent gas motions. For a perturbation with an injection scale of 500 kpc, we have a simple approximation from Gaspari & Churazov (2013), which gives the following:

$$\mathcal{M}_{\rm 3D} \approx 4A_\rho(k_{\rm peak}) \approx 2.4A_P(k_{\rm peak}). \quad (19)$$

This can be generalized to $\mathcal{M}_{\rm 3D} \approx c_\rho A_\rho(k_{\rm peak}) \approx c_P A_P(k_{\rm peak})$, where c_ρ and c_P have a very weak dependence on the injection scale ($\propto \ell_{\rm inj}^{-\alpha_H}$, with $0.2 \lesssim \alpha_H \lesssim 0.3$). For an injection scale of 250 kpc, c_ρ and c_P will be ~20% greater than their values for an injection scale of 500 kpc. Other works find similar linear scalings between fluctuations and Mach numbers; e.g., including the 3D correction $\mathcal{M}_{\rm 3D} = \sqrt{3}\,\mathcal{M}_{\rm 1D}$, Zhuravleva et al. (2023) find a radially averaged relation $\mathcal{M}_{\rm 3D} \approx 2.4\ \delta P/P$.

We might also consider the impact of the cool core of Zwicky 3146. Specifically, for a gas of a given Mach number, we may expect density fluctuations to be significantly higher than pressure fluctuations when radiative cooling is prominent (e.g., Mohapatra et al. 2022). It is not clear how strong the radiative cooling is in Zwicky 3146, as the actual cooling rate may be quenched to ~10% of reported cooling flow rates (see Romero et al. 2020, and references therein). Moreover, the cool core itself has an extent (width) of roughly 20″ (Forman et al. 2002; Giacintucci et al. 2014), so the impact of the cool core on the power spectra in Ring 1 should be negligible.

Khatri & Gaspari (2016) provide a relation between the hydrostatic bias and $\mathcal{M}_{\rm 3D}$, which we denote as $b_{\mathcal{M}}$ when derived from $\mathcal{M}_{\rm 3D}$.

There are several limitations of our data, which inhibit the goal of inferring $b_{\mathcal{M}}$ from thermodynamic fluctuations. Given the commonality of mass estimations at R_{500}, it is desirable to infer $b_{\mathcal{M}}(R_{500})$, but our spectra not being robust in Ring 3 prevents us from being able to do this. Even before then, we have the problem of estimating $\mathcal{M}_{\rm 3D}$ and eventually its (logarithmic) radial slope. As mentioned in Section 4, we cannot determine the peaks of the spectra well, due both to data quality and to the scales accessed in this analysis.

Notwithstanding the above caveats, for spectra that we take to be robust and significant, we calculate Mach numbers and report them in Table 3. These values are all larger than expected for a relaxed cluster (e.g., Zhuravleva et al. 2023). We have deeply explored instrumental systematic errors and biases in our power spectra analyses (see Appendices B and C). We may also call into consideration the assumptions made when modeling our unperturbed cluster, e.g., would an elliptical surface brightness model be more appropriate?

Khatri & Gaspari (2016) provide a relation between the hydrostatic bias and $\mathcal{M}_{\rm 3D}$ (and attach a corresponding subscript to denote the method of calculation, $b_{\mathcal{M}}$):

$$b_{\mathcal{M}} = \frac{-\gamma \mathcal{M}_{\rm 3D}^2}{3} \frac{d \ln P_{\rm NT}}{d \ln P_{\rm th}} \left(1 + \frac{\gamma \mathcal{M}_{\rm 3D}^2}{3} \frac{d \ln P_{\rm NT}}{d \ln P_{\rm th}} \right)^{-1}, \quad (20)$$

Table 3
Inferred Mach Numbers (1) Based on the Peak of the Magnitude Spectra, $\mathcal{M}_{\rm 3D,peak}$ and (2) as Inferred from the Integral of the Spectra (i.e., Variance: σ^2) and Radially Averaged Relations in Zhuravleva et al. (2023), $\mathcal{M}_{\rm 3D,int}$

		$\mathcal{M}_{\rm 3D,peak}$	$\mathcal{M}_{\rm 3D,int}$
Ring 1	$\delta\rho/\rho$	0.53 ± 0.01	0.32
	$\delta P/P$	0.69 ± 0.19	0.80
Ring 2	$\delta\rho/\rho$	0.43 ± 0.14	0.38

where γ is the adiabatic index, taken to be $5/3$ for the ICM. Note that, as defined in Khatri & Gaspari (2016), $b_{\mathcal{M}} \equiv M_x/M_{\rm tot} - 1 = -b$. Following the recasting performed in Khatri & Gaspari (2016), we find

$$\frac{d\ln P_{\rm NT}}{d\ln P_{\rm th}} = \frac{d\ln P_{\rm NT}/d\ln r}{d\ln P_{\rm th}/d\ln r} = 1 + 2\frac{d\ln \mathcal{M}_{\rm 3D}/d\ln r}{d\ln P_{\rm th}/d\ln r}. \quad (21)$$

We can employ the above equation with the average logarithmic pressure slope within Ring 1. Yet, we must also identify a logarithmic Mach number slope ($d\ln \mathcal{M}_{\rm 3D}/d\ln(r)$). Taking the weighted average of the $\mathcal{M}_{\rm 3D,peak}$ values reported in Ring 1 and the X-ray value in Ring 2, we compute a logarithmic slope. Using the weighted average of $\mathcal{M}_{\rm 3D}$ in Ring 1, we obtain $-b_{\mathcal{M}} = 0.16 \pm 0.04$. This value thus represents an estimate of the hydrostatic bias in the central region of the cluster. We note that most estimates of the hydrostatic bias are at a canonical radius like R_{500}, where b is expected to be in the range $0.1 < b < 0.3$ (e.g., Hurier & Angulo 2018). Given the sloshing present in the core, it is plausible that the hydrostatic bias in the central region ($r < 100''$) is of values similar to those expected at R_{500}.

5.3. Ellipticity

There is the potential for a spherical model of an ellipsoidal cluster to impart a bias on the power spectra recovered (e.g., Khatri & Gaspari 2016; Zhuravleva et al. 2023, from the perspectives of observations and simulations, respectively). Indeed, this could apply to our result, where we should expect that our results overestimate the fluctuations at larger scales (i.e., lower k modes). However, the resolution to this problem is not simple, given that, much like in the Coma cluster, the ellipticities can differ between SZ and X-ray, and even between X-ray images, i.e., pn and MOS images (Neumann et al. 2003). As reported in Romero et al. (2020), the ellipticity also varies with radius. So a choice of a single ellipticity would be inherently arbitrary and would itself impart a bias at radii not matching the ellipticity chosen. By extension, employing elliptical fits to surface brightness has also been shown to sufficiently account for substructure such as a shock (e.g., as in RX J1347.5-1145; Di Mascolo et al. 2019) without explicitly modeling the shock itself, hence a fluctuation analysis with such an elliptical model would risk subtracting sought-after fluctuations. Furthermore, there is no clear choice of ellipticity that escapes its own biases. Finally, when deprojecting to 3D quantities, we also introduce a degeneracy in the ellipsoidal shape and inclination of the ellipsoidal relative to the line of sight.

In a broader sense, the question can be asked: "what constitutes the unperturbed cluster model?" It should be a model that follows the shape of the gravitational potential. This question has been raised elsewhere. For example, Zhuravleva et al. (2015) address this by "patching" their β-model of the Perseus cluster, and Sanders & Fabian (2012) fit ellipses to surface brightness contours. In either case, this opens the question of "to what degree of complexity we should go" as well as complicating the interpretation of the underlying 3D distribution of the unperturbed thermodynamic quantities. To answer this accurately requires knowledge about the gravitational potential at a detail that is often not available. We find ourselves in such a position: while our circular surface brightness models are likely not fully sufficient to describe the gravitational potential, we lack the data (or data of sufficient depth) to motivate another specific model instead of choosing a rather arbitrary elliptical model.

6. Conclusions

By leveraging our precursory multiwavelength method (Khatri & Gaspari 2016), in this work we have presented amplitude spectra of surface brightness fluctuations from $\delta S/S$ and $\delta y/y$ images from the X-ray (XMM-Newton) and SZ (MUSTANG-2) data, respectively. The two instruments are well matched in angular resolution, and their sensitivities are conducive to studying the ICM of galaxy clusters at moderate redshift—such as Zwicky 3146 at $z = 0.29$.

Zwicky 3146 is a relaxed, sloshing, cool-core cluster. Our amplitude spectra reflect the sloshing in the core, as the density fluctuations are seen to increase relative to pressure fluctuations at the largest scales in our spectra ($\sim$400 kpc). Our amplitude spectra suggest an injection scale of $140\,{\rm kpc} < \ell_{\rm inj} < 440\,{\rm kpc}$. Our best constraints are in Ring 1, where the X-ray-derived spectra ($\delta\rho/\rho$) suggest an injection scale of $\sim$250 kpc, while the SZ-derived spectra ($\delta P/P$) suggest an injection scale of $\sim$140 kpc. The larger scale from X-rays reflects its sensitivity to a sloshing core. It is conceivable that the SZ data are more sensitive to fluctuations from cavities, where Vantyghem et al. (2021) found potential cavities on the scale of $\sim$50 kpc; such scales are supported by AGN feedback simulations (e.g., Wittor & Gaspari 2020). Our comparison of pressure and density fluctuations in Ring 1 show that, from large to small scales, the ICM equation of state is transitioning from isobaric to adiabatic, with a brief transition through the isothermal regime. This is another sign of increased kinematical motions (Gaspari et al. 2014), corroborating the approach toward the turbulence injection peak potentially at a few tens of kiloparsecs.

In Zwicky 3146, there is no evidence that cavities exist at moderate radii (Ring 2), and in Ring 2, we would expect an injection scale within the scales probed here. We would similarly expect an injection scale within the scales probed for our outermost ring, Ring 3. Unfortunately, neither the X-ray nor SZ data were of sufficient quality to produce reliable constraints in Ring 3. We note that, in the case of SZ data, an instrument with MUSTANG-2 specifications just changing the instantaneous FOV would greatly improve its ability to probe the outskirts of clusters.

Finally, we derive Mach numbers from the 3D spectra by leveraging scalings from hydrodynamical simulations. On average, we infer a turbulent 3D Mach number $\approx$0.5, with the values inferred from pressure fluctuations being relatively larger than those from density fluctuations. From the Mach numbers in the center of the cluster, we infer a hydrostatic bias of $-b_{\mathcal{M}} = 0.16 \pm 0.04$. The uncertainty in these measurements grows rapidly as one probes larger cluster-centric radii. Thus, future deeper and higher-resolution data sets in both X-ray and SZ will be instrumental to fully unveil Zwicky 3146's kinematical state at varying radii and Fourier modes.

Acknowledgments

C.R. is supported by NASA ADAP grant No. 80NSSC19K0574 and Chandra No. grant G08-19117X. C.S. is supported in part by Chandra grant No. GO7-18122X/GO8-19106X and XMM-Newton grant No. NNX17AC69G/80NSSC18K0488. M.G. acknowledges partial support by HST GO-15890.020/023-A, the *BlackHoleWeather* program, and NASA HEC Pleiades (SMD-1726). R.K. acknowledges

support by Max Planck Gesellschaft for Max Planck Partner Group on cosmology with MPA Garching at TIFR and Department of Atomic Energy, Government of India, under Project Identification No. RTI 4002. W.F. acknowledges support from the Smithsonian Institution, the Chandra High Resolution Camera Project through NASA contract NAS8-03060, and NASA grant Nos. 80NSSC19K0116, GO1-22132X, and GO9-20109X. L.D.M. is supported by the ERC-StG "ClustersXCosmo" grant agreement 716762 and acknowledges financial contribution from the agreement ASI-INAF n.2017-14-H.0. The National Radio Astronomy Observatory is a facility of the National Science Foundation operated under cooperative agreement by Associated Universities, Inc. GBT data were taken under the project ID AGBT18A_175. We would like to thank the anonymous reviewer for providing helpful and valuable comments.

Facilities: GBT, XMM.

Software: Astropy (Astropy Collaboration et al. 2013; The Astropy Collaboration 2018), pyproffit (Eckert et al. 2017), emcee (Foreman-Mackey et al. 2013), ESAS (Snowden et al. 2008).

Appendix A
Nonthermal Pressure Profile

Going beyond simply calculating a hydrostatic mass bias, Eckert et al. (2019) attempt to characterize the profile on nonthermal support by assuming a parameterized profile for $P_{\rm NT}/P_{\rm tot}$, the nonthermal pressure divided by the total pressure. One such profile proposed in Nelson et al. (2014) is given as

$$\alpha(r) = \frac{P_{\rm NT}}{P_{\rm tot}}(r) = 1 - A\left(1 + \exp\left\{-\left[\frac{r}{Br_{\rm 200m}}\right]^{\gamma_{\rm NT}}\right\}\right), \tag{A1}$$

where A, B, and $\gamma_{\rm NT}$ are parameters fitted with respective values of 0.452 ± 0.001, 0.841 ± 0.008, and 1.628 ± 0.019 in Nelson et al. (2014). With only R_{500} as a node to constrain this profile, we fix B and $\gamma_{\rm NT}$ to the values from Nelson et al. (2014). For Zwicky 3146, we obtain $R_{\rm 200m} = 2801$ kpc using the NFW Navarro et al. (1996) parameters cited in Klein et al. (2019).

From Eckert et al. (2019), their assumptions yield the following relation:

$$\frac{f_{\rm gas}(r)}{f_{\rm gas,HSE}(r)} = (1 - \alpha)\left(1 - \frac{P_{\rm th} r^2}{(1-\alpha)\rho_{\rm gas} G M_{\rm HSE}} \frac{d\alpha}{dr}\right)^{-1}. \tag{A2}$$

If we adopt the recastings $\alpha(r) = 1 - A * g(r)$ and

$$h(r) = \frac{P_{\rm th} r^2}{\rho_{\rm gas} G M_{\rm HSE}}, \tag{A3}$$

then we can arrange Equation (A2) to solve for the parameter A in the nonthermal pressure fraction profile:

$$A = \frac{f_{\rm gas}(r)}{f_{\rm gas,HSE}(r)}\left(\frac{g - hg'}{g^2}\right), \tag{A4}$$

where $g' = dg/dr$. We find $A = 0.48 \pm 0.2$.

Appendix B
Checks and Biases with the Δ-variance Method

Given that we wrote our own implementation of the power spectrum calculation method presented in Arévalo et al. (2012), we perform several checks to ensure we recover injected spectra as expected. In particular, we adopt an injection spectrum, $P_{\rm inj}$ of the form

$$P_{\rm inj} = P_0 e^{-k_c/k} k^{-\alpha}, \tag{B1}$$

where k_c is a cutoff wavenumber (toward low values), P_0 is a normalization, and α is the power-law index. The value of P_0 is arbitrary for our checks. Similarly, noise realizations are created as images with more pixels than in our SZ or X-ray maps, and the units of the pixels is arbitrary. However, we do check proper handling of the value of the pixel size. We test the recovery of the injected spectrum within the range of $0 \leqslant \alpha \leqslant 11/3$, where $\alpha = 11/3$ is realistically steeper than expected in 2D. We find excellent recovery of the shape (see Figure 13).

From Arévalo et al. (2012), the expected normalization bias in the recovered spectrum, P_k is

$$\frac{P_k}{P_{\rm inj}} = 2^{\alpha/2}\frac{\Gamma(n/2 + 2 - \alpha/2)}{\Gamma(n/2 + 2)}, \tag{B2}$$

where n is the number of dimensions of the data, which in our case is 2. As noted in Arévalo et al. (2012), for the 2D (and 3D) case, the bias is modest in the range $0 < \alpha < 3$, where this range encompasses expected slopes of surface brightness fluctuations. In particular, we note that the expected bias is exactly unity at $\alpha = 0$ and $\alpha = 2$. For $\alpha = 3.7$, the expected bias is 1.68 and we find a bias value of 1.66 at the highest k value sampled. That is, our recovered normalization agrees very well with expectations.

B.1. Bias for an Image Smoothed by a Multi-Gaussian Kernel

Arévalo et al. (2012) derive their bias by calculating V_{k_r}, the variance of the filtered image as properly integrated and approximately integrated. That is, for $\tilde{F}_{k_r}(k)$ as the Fourier transform of the filter, they evaluate

$$V_{k_r} = \int P(k)|\tilde{F}_{k_r}(k)|^2 d^n k, \tag{B3}$$

first with $P(k)$ inside the integral (proper integration) and again after moving $P(k)$ outside of the integral (approximate integration), and then find the ratio between the two.

To derive the appropriate bias for a smoothed image, let us first note that, from the convolution theorem, we have

$$P(k) = P_{\rm u}(k) P_{\rm PSF}(k) = P_0 k^{-\alpha} P_{\rm PSF}(k), \tag{B4}$$

where $P(k)$ is the power spectrum of the smoothed image, $P_{\rm u}(k)$ is the power spectrum of the unsmoothed image, and $P_{\rm PSF}(k)$ is the power spectrum of the PSF. In order to retain a similar ability to integrate the expression in Equation (B3), we opt to characterize the PSF as the stack of multiple Gaussians. In our case, we will define a radially symmetric multi-Gaussian, composed of N Gaussians, as

$$G_{\rm multi} = \sum_{i=1}^{N} c_i e^{-\boldsymbol{x}^2/(2\sigma_i^2)}, \tag{B5}$$

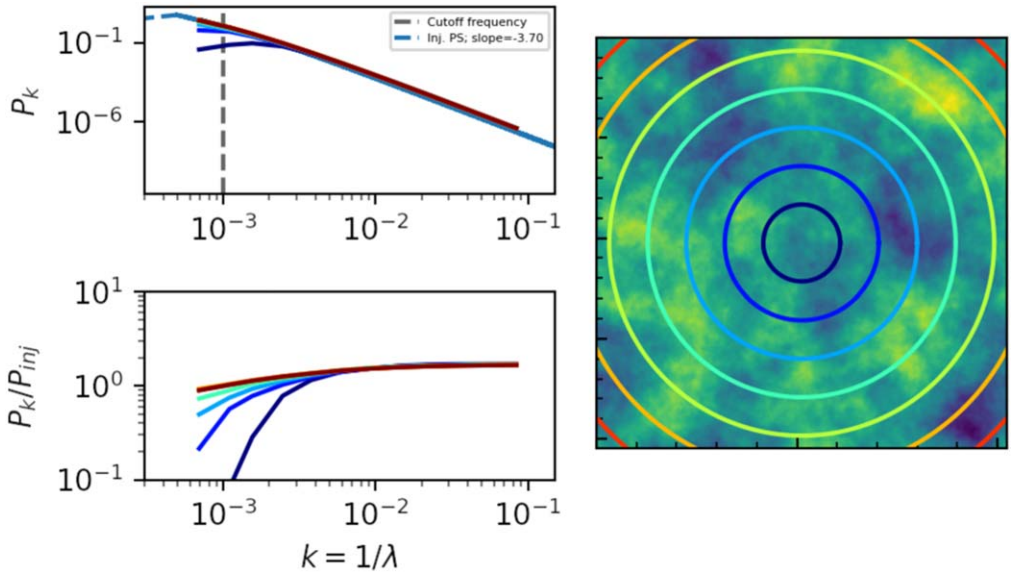

Figure 13. The recovered power spectra (denoted "MH PS") of injected power spectra (blue dots, forming a thick line) with different masks ($r <$ rmax) used. The color lines in the plots have corresponding circles drawn in the right panel. The MH filter quickly recovers low-k values; the cutoff wavenumber, k_c, is indicated by the vertical dashed line. We find very good agreement with the expected normalization bias of this method (see Appendix B in Arévalo et al. 2012).

where c_i is the normalization of each Gaussian such that the total normalization is equal to unity, i.e., $\sum c_i = 1$. The Fourier transform of this multiple Gaussian is itself a multiple Gaussian:

$$\tilde{G}_{\rm multi} = \int G_{\rm multi}\, e^{-i2\pi \boldsymbol{x}\boldsymbol{k}} d^n x = \sum_{i=1}^{N} c_i e^{-k^2/k_i^2}, \tag{B6}$$

where $k_i = 1.0/(\sqrt{2}\,\pi\sigma_i)$. We can further define $k_i = x_i * k_r$. If we then take $P_{\rm PSF}(k) = \tilde{G}^2_{\rm multi}$, Equation (B3) now becomes

$$V_{k_r} = \int P_{\rm u}(k) \left[\sum_{i=1}^{N}\sum_{j=1}^{N} c_i c_j e^{-k^2/k_i^2} e^{-k^2/k_j^2} \right] \times \left[2\epsilon \left(\frac{k}{k_r}\right)^2 e^{-(k/k_r)^2} \right]^2 d^n k \tag{B7}$$

$$= \sum_{i=1}^{N}\sum_{j=1}^{N} 4\epsilon^2 \int P_{\rm u}(k) c_i c_j e^{-k^2/(x_i k_r)^2} e^{-k^2/(x_j k_r)^2} \times \left(\frac{k}{k_r}\right)^4 e^{-2(k/k_r)^2} d^n k, \tag{B8}$$

and via the same variable recasting, we derive a new bias formulation:

$$\frac{\tilde{P}}{P}(k_r) = 2^{\alpha/2} \left[\sum_{i=1}^{N}\sum_{j=1}^{N} c_i c_j \left(\frac{2x_i^2 x_j^2 + x_i^2 + x_j^2}{2x_i^2 x_j^2} \right)^{n/2+2-\alpha/2} \right] \times \frac{\Gamma(n/2+2-\alpha/2)}{\Gamma(n/2+2)}. \tag{B9}$$

B.1.1. Application to the Point-spread Functions of the EPIC Cameras

In order to infer our induced biases for XMM images, we will approximate the PSFs of our images as triple Gaussians.

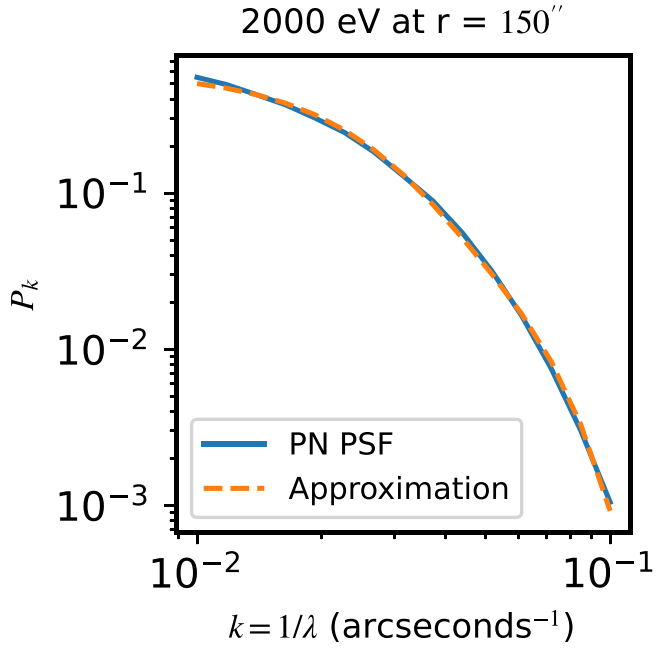

Figure 14. Triple Gaussian approximation of the XMM PSF(s). Triple Gaussians are fit to the appropriate PSF per detector, energy band, and radius; the fit is over the selected range ($0.01 < k \times$ arcsec<0.1; we need not worry if the approximation deviates from the true PSF outside of this range.

From Section 3.2, we adopt a single PSF for each ring [3], each detector [3], and each energy band [2]. (Given that the three observations are well-centered on the cluster, we need not treat PSFs differently between the three observations, i.e., ObsIDs). We thus have $3 \times 3 \times 2 = 18$ different PSFs to which we fit triple Gaussians, where the fit is actually a direct fit to the power spectra of the PSFs. Figure 14 shows that the triple Gaussian approximation stays very tight to the measured PSF; this is true for each of the 18 PSFs and respective approximations.

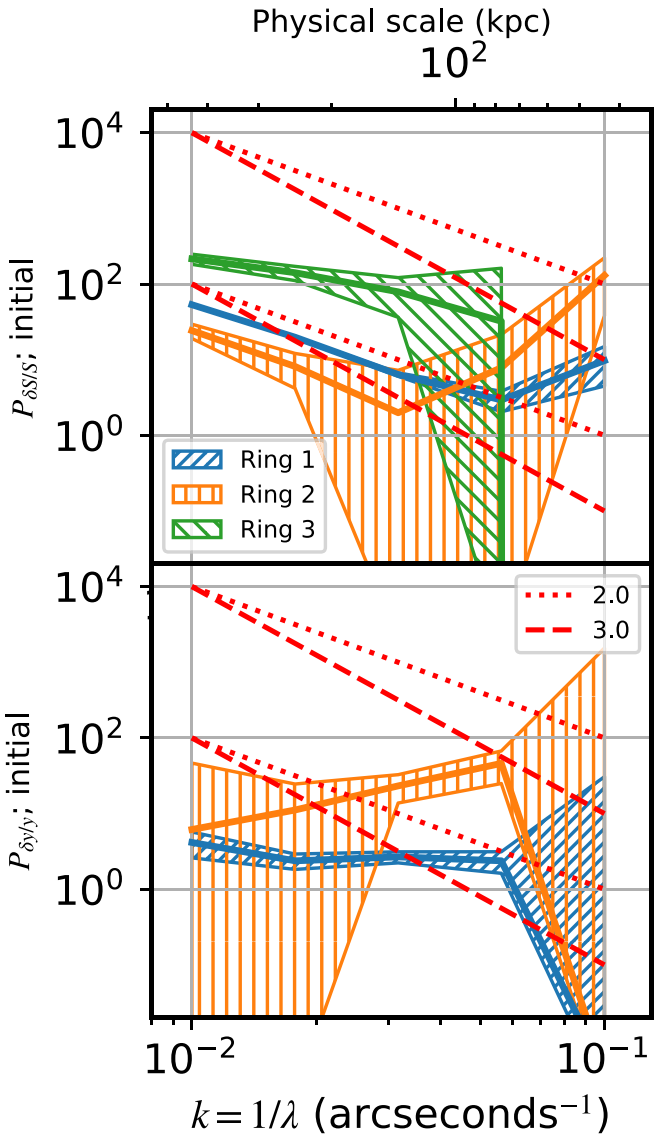

Figure 15. Initial inference of $P_u(k)$ for XMM (top panel) and MUSTANG-2 (bottom panel) without a bias correction. Dashed red lines show a power-law slope $\alpha = 3$ ($P \propto k^{-\alpha}$), and dotted red lines correspond to $\alpha = 2$. The steepest values we see in the X-ray spectra are $\alpha \approx 3$, and for the SZ spectra, $\alpha \approx 2$.

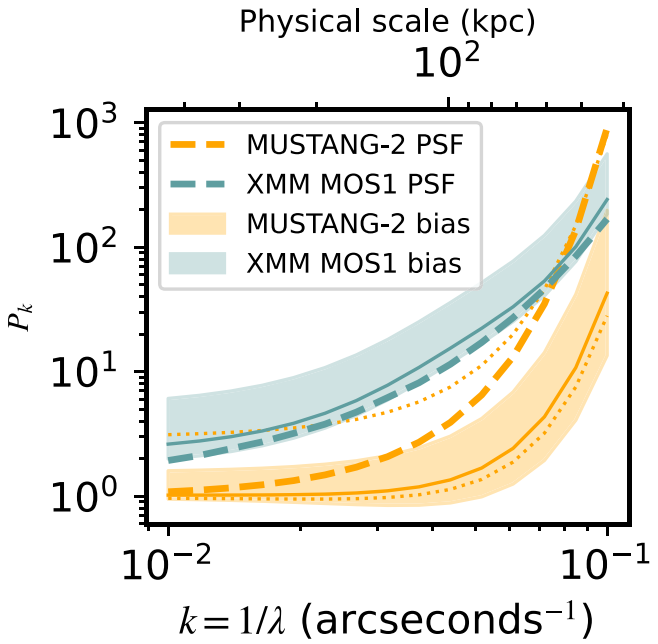

Figure 16. The bias induced by PSF convolution (shaded regions and solid lines) in comparison to the inverse of the power spectra of PSFs (dashed lines) for XMM and MUSTANG-2. To illustrate the bias for XMM, we have only plotted the PSF of MOS1 at 800 eV bin at $r = 150''$. The solid lines indicate the bias when $\alpha = 3$ for XMM and $\alpha = 2$ for MUSTANG-2. The shaded regions encompass the bias between $\alpha = 1.5$ and $\alpha = 4.5$ for XMM, and between $\alpha = 0.5$ and $\alpha = 3.5$ for MUSTANG-2. For a full comparison, the orange dotted lines show the biases for $\alpha = 1.5$ and $\alpha = 4.5$ with the MUSTANG-2 beam.

For MUSTANG-2, it has been standard to calculate its beam (PSF) as a double Gaussian (see Romero et al. 2015, 2017, 2020).

We require yet another assumption before estimating our induced bias, that being the underlying spectral index. One starting point is that we could assume a Kolmogorov spectrum of $\alpha = 11/3$. However, we do not expect a single spectral index across all scales (e.g., Gaspari et al. 2014). At the scales probed, we should expect the slopes to only steepen toward larger k. Thus, we can perform an initial recovery of power spectra and identify the steepest slope between our nodes. That is, we will expect our initial spectra to show shallower slopes toward higher k, due to the increasing bias.

The 2D spectra from MUSTANG-2 are calculated as outlined in Section 3.1 and for XMM as in Section 3.2, where we note that the XMM spectra presented in Figure 15 are the weighted averages of the 18 different images per ring (recall there are three ObsIDs with usable EPIC data). We find that the steepest slopes in the X-ray data are steeper than $\alpha \approx 3$, while for the SZ data they are just slightly steeper than $\alpha \approx 2$. We take a slightly arbitrary uncertainty range of ± 1.5 about these indices, such that for X-rays we consider biases from $\alpha = 3 \pm 1.5$, and from SZ we consider biases from $\alpha = 2 \pm 1.5$. The inferred biases are shown via solid lines and shaded regions in Figure 16.

Appendix C
Detailed Power Spectra Implementation

The power spectra in Section 3 focus on the fractional residual maps ($\delta y/\bar{y}$ or $\delta S/\bar{S}$). However, both the power spectra from SZ (MUSTANG-2) and X-ray (XMM) data must both have their noise bias removed. From the auto power spectrum, this would be achieved as

$$P_{\delta y/\bar{y}} = P_{\delta y/\bar{y},\mathrm{raw}} - P_{\delta y/\bar{y},\mathrm{noise}}, \quad \text{or} \tag{C1}$$

$$P_{\delta S/\bar{S}} = P_{\delta S/\bar{S},\mathrm{raw}} - P_{\delta S/\bar{S},\mathrm{noise}}, \tag{C2}$$

where the raw spectra are calculated on the fractional residual, and the noise power spectrum on the associated noise realization.

An alternative is to take a cross-spectrum. To do this, we alter the standard calculation of the variance. In the framework of the delta-variance approach used, an important intermediate product is the filtered image, $\tilde{I}_k$:

$$\tilde{I}_k(\theta) = \left(\frac{G_{\sigma_1} * I}{G_{\sigma_1} * M} - \frac{G_{\sigma_2} * I}{G_{\sigma_2} * M} \right) M, \tag{C3}$$

where M is the mask, I is the image, and G_σ are Gaussian kernels with corresponding widths σ_1 and σ_2. For n

dimensions, the variance is given as

$$V_k = \frac{N}{N_{M=1}} \times \int \tilde{I}_k^2 d^n x, \tag{C4}$$

where $N = \int d^n x$ and $N_{M=1} = \int M(x) d^n x$. In the case of calculating a cross-spectrum, we have two images, I_a and I_b, which when filtered become $\tilde{I}_a$ and $\tilde{I}_b$. The variance for the cross-spectrum term is then

$$V_k = \frac{N}{N_{M=1}} \times \int (\tilde{I}_a \times \tilde{I}_b) d^2 x, \tag{C5}$$

where we explicitly note that we have two-dimensional images in this work.

The uncertainties in $P_{\delta y/\bar{y}}$ and $P_{\delta S/\bar{S}}$ are calculated in very similar ways. That is, if noise realizations are made to determine $P_{\delta y/\bar{y},\mathrm{noise}}$ and $P_{\delta S/\bar{S},\mathrm{noise}}$, where these quantities are taken as the mean power spectra across noise realizations, then the standard deviation of the respective noise power spectra can be taken as the uncertainty in the noise power spectra. Using x as a stand-in for y or S, we have

$$\sigma_{P_{\delta x/\bar{x}}} = \sigma_{P_{\delta x/\bar{x},\mathrm{noise}}}, \tag{C6}$$

$$\sigma_{A_{\delta x/\bar{x}}} = \sigma_{P_{\delta x/\bar{x}}}/(2A_{\delta x/\bar{x}}). \tag{C7}$$

C.1. MUSTANG-2 Error Estimation

The MUSTANG-2 map of Zwicky 3146 is comprised of 155 individual scans on source. We reprocess each scan, subtracting the full model that was fit in Romero et al. (2020). These scans span seven observing nights. To create 100 realizations of pairs of half maps, we randomly select half of the 155 scans to assign to "half 1" and the rest to "half 2." The cross-spectra are calculated as noted above. The mean and standard deviation of power spectra are respectively taken as the expected $P_{2\mathrm{D}}$ value and associated uncertainty.

C.2. XMM Error Estimation

Our XMM noise realizations are fundamentally generated as Poisson noise with a model of the counts image as the mean value for each pixel. The simplest model is

$$C = \bar{S} * E + \bar{B}, \tag{C8}$$

where $\bar{S}$ is our (smooth) ICM model (taken as a circular double β model; see Equation (3)), E is the exposure map, and $\bar{B}$ is a background, which itself has multiple components. We can separate $\bar{B}$ as

$$\bar{B} = \bar{B}_p + \bar{B}_{\mathrm{CXB}} + \bar{B}_F + \bar{B}_{\mathrm{pt.\ srcs}}, \tag{C9}$$

where $\bar{B}_p$ is a model of the particle background, soft proton, and for the pn detector, the OOT contribution. $\bar{B}_{\mathrm{CXB}}$ is taken to be the uniform background (when looking at count rates) level when fitting for the ICM profile. $\bar{B}_F$ is the fluorescent background, which has a profile proportional to the unvignetted exposure divided by the vignetted exposure. $\bar{B}_{\mathrm{pt.\ srcs}}$ is an estimate of faint point sources.

Our initial image of B_p is formed by the addition of various image outputs from the ESAS framework, and itself is subject to Poisson noise. To lessen this in the model itself, we smooth

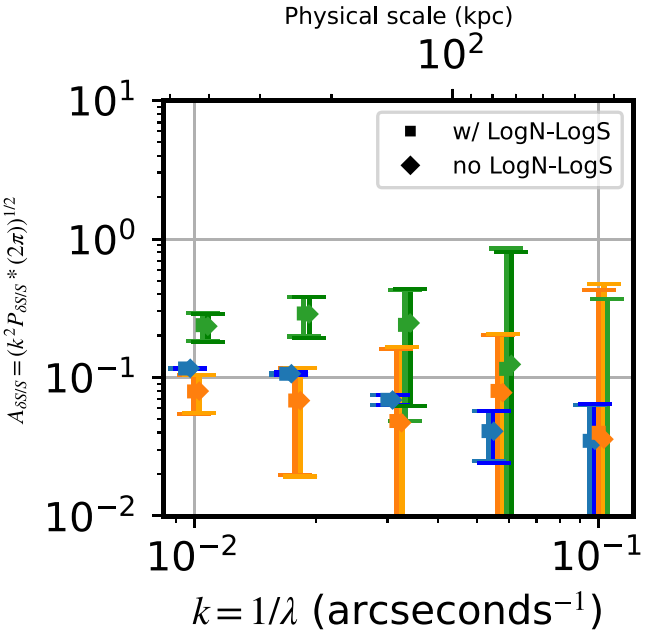

Figure 17. There is a negligible difference with respect to our treatment of faint sources.

it, initially as

$$\bar{B}_p = \left(\frac{G_{2.5} * B_{\mathrm{p}}}{G_{2.5} * E}\right) \times E, \tag{C10}$$

where $G_{2.5}$ is a Gaussian kernel of 2.5 pixels (pixels themselves are 2.″5). This method should account for "losses" in chip gaps. Though this is likely sufficient, we attempt to fill in chip gaps with the mean values of neighboring non-gap values. To do this, we iterate the smoothing; at each iteration, the non-gap values are restored to their original values, while the gap pixels are kept from the previous iteration. As the gaps are not wide, this converges quickly. Our final $\bar{B}_p$ image is obtained as

$$\bar{B}_p = \left(\frac{G_{2.5} * B_{\mathrm{p,gap-filled}}}{G_{2.5} * E}\right) \times E. \tag{C11}$$

The remaining smooth background components are calculated as

$$\bar{B}_{\mathrm{CXB}} = 10^{b_{\mathrm{uni}}} * E, \tag{C12}$$

where b_{uni} is the parameter fit (in logarithmic space) for the uniform background, and

$$\bar{B}_f = 10^{b_{\mathrm{f}}} * \frac{E_{\mathrm{unv}}}{E} E, \tag{C13}$$

where b_{f} is the fitted parameter (in logarithmic space) for the fluorescent background and E_{unv} is the unvignetted exposure.

If we include point sources, i.e., $\bar{B}_{\mathrm{pt.\ srcs}}$, we do so as indicated in Section 3.2. That is, we match a Log N–Log S distribution to the distribution calculated (observed) in each image using bright sources, where the completeness is approximately unity, and assume an index of -1.6. As we are taking spectra only within a circle of radius 5′ about the center of the cluster, we generate model point sources only in this region, and we assume a uniform PSF for a given detector and energy band. In particular, we adopt the PSF at $x = 150''$ and $y = 0$ generated by `psfgen` as noted in Section 3. The

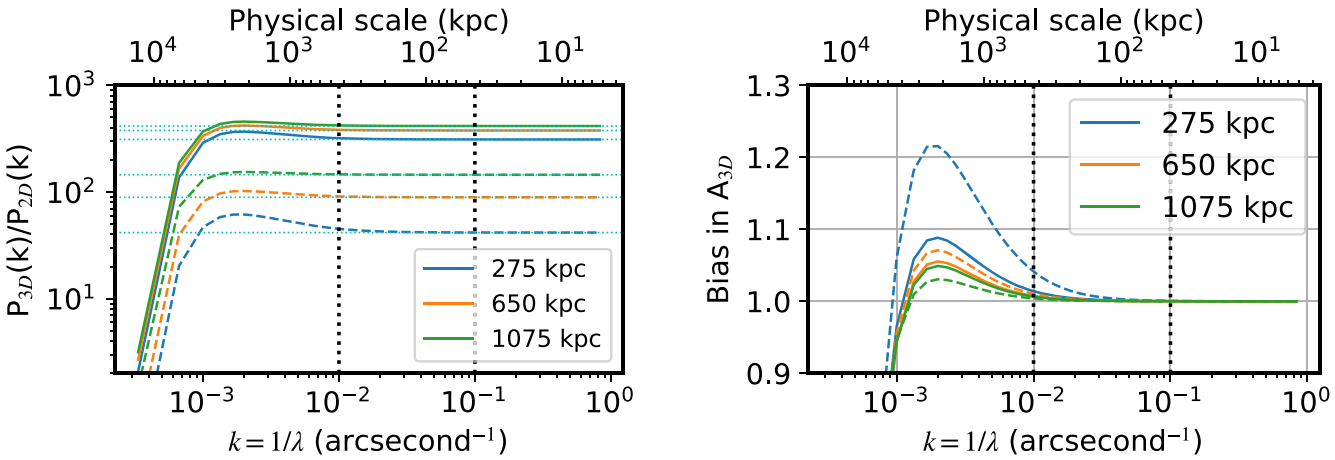

Figure 18. Ratios of power spectra (above) and amplitude spectra (below) when calculated via Equation (6) assuming a power-law distribution as in Equation (B1) with $k_c = 1e-3$ kpc^{-1} and $\alpha = 3$. Solid lines show the ratios when applying the SZ window function, and dashed lines show the ratios when applying the X-ray window function. The horizontal (dotted cyan) lines in the above panel show the approximate ratios between the 3D and 2D power spectra as approximated in Equations (11) and (12). The chosen radii are close to the effective radii (weighted averages) for N of both the SZ and X-ray window functions for Rings 1, 2, and 3, respectively.

mean photon count rate from the model point sources within 5′ of the cluster center is calculated and then subtracted from the same region in $\bar{B}_{\rm CXB}$.

We wish to include covariance of our profile fit in our estimation of uncertainties in power spectra. Accordingly, we will have many models C, such that each noise realization is generated from an instance, C_i, with relevant components being dictated from chains of the profile fits. Specifically, $\bar{S}$, $\bar{B}_{\rm CXB}$, and $\bar{B}_f$ depend on the chains and change with each realization.

We find that the inclusion of faint point sources barely affects our power spectra, as evidenced in Figure 17. Even so, the results presented in this paper include an estimated contribution from such faint point sources.

C.3. Validation of Deprojection Approximation

With window functions in hand, we can easily validate our approximate power spectra deprojection (Equation (9)) against the initial formulation, i.e., Equation (6).

The slopes found in our data (see Table 2) are generally shallower than expected, with the steepest slope being 2.4 in Ring 1. From Figure 18, we can conservatively say that we potentially underestimate the density fluctuation at $k = 0.01$ arcsecond^{-1} by $\sim$1.05 (assuming the slope may be roughly 3 as we approach those scales).

C.4. Correlated Noise on Small Scales

We investigate if the increase in the amplitude spectra toward higher k may be due to correlated noise on small scales. One particular investigation is the potential for secondary particles generated from collisions of cosmic rays and the telescope. If striking a detector, such secondary particles would do so effectively simultaneously. Thus, in the X-ray data, this could be seen as multiple events in a single frame. To avoid also counting multiple events from bright sources, we mask the cluster and point sources; we also perform this analysis while filtering energies in our two adopted bands (400–1250 eV and 1250–5000 eV).

Wanting the shortest frame for this analysis, we analyze the pn detector from the only full-frame observation (0108670101) where the time resolution is 73.4 ms. When counting the number of events per frame, we find at most three events per frame; in the high-energy band, only 5% of the events in this observation occur in the same frame as another event. The distances between these events are then binned as seen in Figure 19 (blue bars). To compare to what a random distribution would be (given our mask), we perform the same calculation but randomly shuffling the events by time (orange step plot). We consider any events occurring within 50″ to be at "short distance." The excess short-distance events account for 9% of the total pairs. We infer that the occurrence of events from (hypothesized) particle showers accounts for less than 0.4% of high-energy events in the background. Repeating this analysis for the low-energy band, we find that only 0.2% of events could be due to such particle showers. Thus, we do not find evidence that this effect could account for a rise toward higher k in the recovered amplitude spectra from X-ray surface brightness fluctuations.

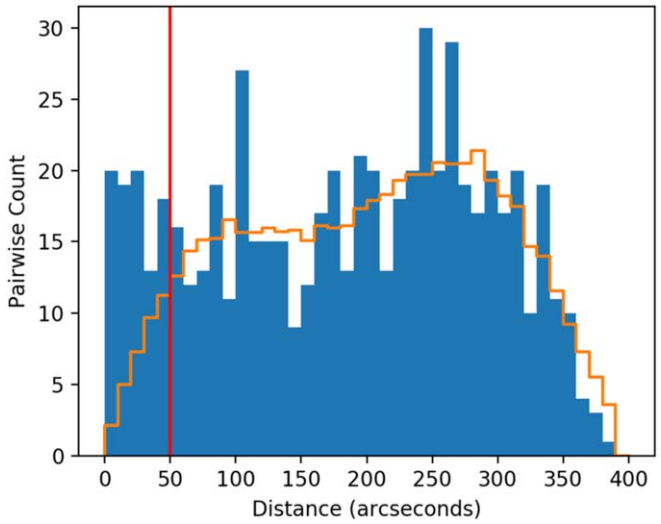

Figure 19. Histogram of distances between pairs of events in the same frame as seen in our actual data (blue) and averaged over 100 realizations in which the event times are randomly shuffled.

ORCID iDs

Charles E. Romero https://orcid.org/0000-0001-5725-0359
Massimo Gaspari https://orcid.org/0000-0003-2754-9258
Gerrit Schellenberger https://orcid.org/0000-0002-4962-0740
Tanay Bhandarkar https://orcid.org/0000-0002-2971-1776
Mark Devlin https://orcid.org/0000-0002-3169-9761
Simon R. Dicker https://orcid.org/0000-0002-1940-4289
William Forman https://orcid.org/0000-0002-9478-1682
Ralph Kraft https://orcid.org/0000-0002-0765-0511
Luca Di Mascolo https://orcid.org/0000-0003-3586-4485
Brian S. Mason https://orcid.org/0000-0002-8472-836X
Emily Moravec https://orcid.org/0000-0001-9793-5416
Tony Mroczkowski https://orcid.org/0000-0003-3816-5372
Paul Nulsen https://orcid.org/0000-0003-0297-4493
John Orlowski-Scherer https://orcid.org/0000-0003-1842-8104
Craig Sarazin https://orcid.org/0000-0003-0167-0981
Jonathan Sievers https://orcid.org/0000-0001-6903-5074
Yuanyuan Su https://orcid.org/0000-0002-3886-1258

References

Allen, S. W., Edge, A. C., Fabian, A. C., et al. 1992, MNRAS, 259, 67
Arévalo, P., Churazov, E., Zhuravleva, I., Forman, W. R., & Jones, C. 2016, ApJ, 818, 14
Arévalo, P., Churazov, E., Zhuravleva, I., Hernández-Monteagudo, C., & Revnivtsev, M. 2012, MNRAS, 426, 1793
Astropy Collaboration, Robitaille, T. P., Tollerud, E. J., et al. 2013, A&A, 558, A33
Bourdin, H., Mazzotta, P., Kozmanyan, A., Jones, C., & Vikhlinin, A. 2017, ApJ, 843, 72
Cho, H., Ryu, D., & Kang, H. 2022, ApJ, 926, 183
Churazov, E., Vikhlinin, A., Zhuravleva, I., et al. 2012, MNRAS, 421, 1123
De Luca, A., & Molendi, S. 2004, A&A, 419, 837
Di Mascolo, L., Churazov, E., & Mroczkowski, T. 2019, MNRAS, 487, 4037
Dicker, S. R., Romero, C. E., Di Mascolo, L., et al. 2020, ApJ, 902, 144
Drake, J. F., Pfrommer, C., Reynolds, C. S., et al. 2021, ApJ, 923, 245
Eckert, D., Gaspari, M., Vazza, F., et al. 2017, ApJL, 843, L29
Eckert, D., Ghirardini, V., Ettori, S., et al. 2019, A&A, 621, A40
Foreman-Mackey, D., Hogg, D. W., Lang, D., & Goodman, J. 2013, PASP, 125, 306
Forman, W., Donnelly, H., Markevitch, M., et al. 2002, HiA, 12, 504
Gaspari, M., Brighenti, F., & Ruszkowski, M. 2013, AN, 334, 394
Gaspari, M., & Churazov, E. 2013, A&A, 559, A78
Gaspari, M., Churazov, E., Nagai, D., Lau, E. T., & Zhuravleva, I. 2014, A&A, 569, A67
Gaspari, M., Tombesi, F., & Cappi, M. 2020, NatAs, 4, 10
Giacintucci, S., Markevitch, M., Venturi, T., et al. 2014, ApJ, 781, 9
Hilton, M., Hasselfield, M., Sifón, C., et al. 2018, ApJS, 235, 20
Hofmann, F., Sanders, J. S., Nandra, K., Clerc, N., & Gaspari, M. 2016, A&A, 585, A130
Hurier, G., & Angulo, R. E. 2018, A&A, 610, L4
Khatri, R., & Gaspari, M. 2016, MNRAS, 463, 655
Klein, M., Israel, H., Nagarajan, A., et al. 2019, MNRAS, 488, 1704
Martino, R., Mazzotta, P., Bourdin, H., et al. 2014, MNRAS, 443, 2342
Mateos, S., Warwick, R. S., Carrera, F. J., et al. 2008, A&A, 492, 51
Mohapatra, R., Federrath, C., & Sharma, P. 2022, MNRAS, 514, 3139
Nandra, K., Barret, D., Barcons, X., et al. 2013, arXiv:1306.2307
Navarro, J. F., Frenk, C. S., & White, S. D. M. 1996, ApJ, 462, 563
Nelson, K., Lau, E. T., & Nagai, D. 2014, ApJ, 792, 25
Neumann, D. M., Lumb, D. H., Pratt, G. W., & Briel, U. G. 2003, A&A, 400, 811
Orlowski-Scherer, J., Haridas, S. K., Di Mascolo, L., et al. 2022, A&A, 667, L7
Peacock, J. A. 1999, Cosmological Physics (Cambridge: Cambridge Univ. Press)
Romero, C. E., Mason, B. S., Sayers, J., et al. 2015, ApJ, 807, 121
Romero, C. E., Mason, B. S., Sayers, J., et al. 2017, ApJ, 838, 86
Romero, C. E., Sievers, J., Ghirardini, V., et al. 2020, ApJ, 891, 90
Roncarelli, M., Gaspari, M., Ettori, S., et al. 2018, A&A, 618, A39
Sanders, J. S., & Fabian, A. C. 2012, MNRAS, 421, 726
Schuecker, P., Böhringer, H., Collins, C. A., & Guzzo, L. 2003, A&A, 398, 867
Snowden, S. L., Mushotzky, R. F., Kuntz, K. D., & Davis, D. S. 2008, A&A, 478, 615
Sunyaev, R. A., & Zel'dovich, Y. B. 1970, CoASP, 2, 66
Sunyaev, R. A., & Zel'dovich, Y. B. 1972, CoASP, 4, 173
The Astropy Collaboration 2018, astropy v3.0.5: A Core Python Package for Astronomy, v3.0.5, Zenodo, doi:10.5281/zenodo.1461536
Vantyghem, A. N., McNamara, B. R., O'Dea, C. P., et al. 2021, ApJ, 910, 53
Wittor, D., & Gaspari, M. 2020, MNRAS, 498, 4983
XRISM Science Team 2020, arXiv:2003.04962
Zhuravleva, I., Allen, S. W., Mantz, A., & Werner, N. 2018, ApJ, 865, 53
Zhuravleva, I., Chen, M. C., Churazov, E., et al. 2023, MNRAS, 520, 5157
Zhuravleva, I., Churazov, E., Arévalo, P., et al. 2015, MNRAS, 450, 4184
Zhuravleva, I., Churazov, E., Kravtsov, A., & Sunyaev, R. 2012, MNRAS, 422, 2712
Zhuravleva, I., Churazov, E., Schekochihin, A. A., et al. 2014, Natur, 515, 85